

UNIVERSIDAD TECNICA
FEDERICO SANTA MARIA

Department of Civil Engineering

Estimating Nearshore Wave Forcing Using Remote Sensing Data: A Case Study at the Maipo River Mouth

A Thesis Submitted in Partial Fulfillment of the Requirements for

Sebastián Véliz Cuéllar

the Professional Title of

Civil Engineer

and the Degree of

Master of Science in Civil Engineering

Thesis Advisor
Raúl Flores Audibert

October, 2026

CONSTANCIA DE VALIDACIÓN Y CONFIDENCIALIDAD DE MONOGRAFÍA A REPOSITORIO ACADÉMICO

1.- IDENTIFICACIÓN DEL TRABAJO ACADÉMICO

Tipo de monografía (marcar una opción): ☐ Memoria o trabajo de título ☒ Tesis de Postgrado

Título del trabajo: ESTIMACIÓN DE FORZANTES DE OLEAJE A PARTIR DE MEDICIONES REMOTAS: CASO APLICACIÓN DESEMBOCADURA RÍO MAIPO.

Nombre del candidato(a): Sebastián Arturo Véliz Cuéllar.

Carrera / Grado: Ingeniería Civil / Magíster en Ciencias de la Ingeniería Civil.

Campus: Casa Central, Valparaíso. **Departamento:** Obras Civiles, Magíster en Ciencias de la Ingeniería Civil.

2.- VALIDACIÓN DEL PROFESOR GUÍA/DIRECTOR DE TESIS

Yo, Raúl Pedro Flores Audibert, en mi calidad de profesor(a) guía/director(a) del trabajo académico mencionado anteriormente **DEJO CONSTANCIA** que:

- He revisado esta versión del documento y corresponde a la versión final aprobada del trabajo.
- El trabajo cumple con los requisitos académicos y de formato establecidos por la institución.

3.- EVALUACIÓN DE CONFIDENCIALIDAD POR PROPIEDAD INDUSTRIAL (marcar una opción)

☒ El trabajo **NO contiene** información que amerite confidencialidad y puede ser publicado de inmediato en repositorio con acceso abierto.

☐ El trabajo **CONTIENE** información con potenciales implicancias de propiedad industrial o intelectual y requiere un periodo de confidencialidad (**embargo**) por **(marcar una opción)**:

☐ 6 meses ☐ 12 meses ☐ 2 años ☐ 3 años ☐ 5 años ☐ 10 años

Fundamentación de la necesidad de confidencialidad (obligatorio si se solicita embargo):

4.- FIRMAS

Profesor(a) guía o director(a) de memoria o tesis: Raúl Flores Audibert.

Fecha: 29/10/2026 **Firma:**

Estudiante o Candidato(a): Sebastián Véliz Cuéllar.

Fecha: 29/10/2026 **Firma:**

Estimating Nearshore Wave Forcing Using Remote Sensing Data: A Case Study at the Maipo River Mouth

Sebastián A. Véliz[1], Raúl P. Flores[1], Patricio A. Catalán[1,2], Francisco J. Sáez[2]

[1] Department of Civil Engineering, Universidad Técnica Federico Santa María, Valparaíso, Chile
[2] Research Center for Integrated Disaster Risk Management (CIGIDEN R+), Santiago, Chile

Abstract

Quantifying wave-induced forcing and energy dissipation in dynamic river–wave interaction zones is essential for coastal morphodynamics, yet traditional approaches face severe observational bottlenecks due to hazardous surf zone conditions and numerical model reliance on rapidly outdated bathymetry. This study introduces a non-intrusive observational framework that integrates UAV imagery, deep learning semantic segmentation (U-Net), and spatiotemporal kinematic tracking to continuously resolve surf zone hydrodynamic forcing directly from surface optical footprints. By targeting the characteristic spatial morphology and texture of active breaking rollers, the convolutional architecture isolates active breaking zones across optically complex backgrounds, mitigating false detections commonly induced by sediment-laden estuarine plumes and persistent remnant foam. The framework successfully isolates wave-by-wave instantaneous mechanics from sea-state phase-averaged dissipation, revealing how wave climate characteristics fundamentally govern nearshore hydrodynamic coupling. Under organized long-period swell, a strong linear coupling binds roller footprint, breaking probability, and total energy dissipation. Conversely, steeper wave climates promote localized plunging breakers that decouple physical roller size from energy flux, shifting geometric scale controls toward local wave celerity. By utilizing only a static baseline bathymetry to establish representative bed slopes and kinematic tracking thresholds—thereby circumventing the need for continuously updated bathymetric inputs to compute energy fluxes—this methodology establishes a robust, observation-driven paradigm for operational monitoring, depth inversion, and hazard assessment in rapidly evolving coastal-riverine environments.

Keywords: Roller, Wave breaking, Wave phase velocity, Dissipation, Wave forcing.

Contents

1 Introduction **6**

2 Objectives and Hypotheses **8**
2.1 General Objective 8
2.2 Specific Objectives 8
2.3 Hypotheses 9

3 Methodology **10**
3.1 Roller Force Estimation 10
3.2 Data Curation 11
3.3 Wave breaking detection 13
3.4 Energy Dissipation by Wave Breaking Estimation 14
3.5 Kinematic Characterization: Celerity and Propagation Direction 18

4 Study Cases **21**

5 Results **23**
5.1 Scenario 1: High-Energy Oblique Swell ($H_s = 1.71\,\mathrm{m}$, $T_p = 12.80\,\mathrm{s}$, $\theta_p = 296.8°$) . . . 23
5.2 Scenario 2: High-Energy Shore-Normal Swell ($H_s = 1.71\,\mathrm{m}$, $T_p = 10.24\,\mathrm{s}$, $\theta_p = 271.6°$) 25
5.3 Cross-Scenario Hydrodynamic Synthesis 26

6 Discussion **28**
6.1 Robustness and Qualitative Assessment of Semantic Segmentation in Heterogeneous Optical Environments 28
6.2 Spatiotemporal Discretization and Velocity Quantization Limits 29
6.3 Calibration and Validation of UAV-derived Wave Celerity 30
6.4 Spatially Resolved Wave Propagation and Estuarine Wave-Current Interactions . . . 33
6.5 Statistical Validation and Analysis of Mean Wave-by-Wave Dissipation ($\bar{D}_{\mathrm{inst}}$) 33
6.6 Wave Climate Controls on Surf Zone Kinematics and Dynamic Coupling: Spatial Correlation and Variance Decomposition 35

7 Conclusions **40**
7.1 Trade-Off Analysis: Optical Remote Sensing vs. Process-Based Numerical Modeling 41
7.2 Avenues for Future Research 41

List of Figures

1 Flowchart of the automated methodology for estimating breaking wave roller force and energy dissipation. The algorithmic structure comprises three main modules: continuous roller tracking and celerity estimation (green), wave propagation direction assessment for dissipated rollers (grey), and spatial energy dissipation computation applying Duncan's formulation (orange). Tracking fidelity is governed by a physical control filter that compares the measured centroid celerity (C_m) against a theoretical threshold (C_{th}) derived from Linear Wave Theory. 12

2 Sequential visualization of the proposed image processing pipeline: (a) raw RGB aerial frame; (b) radiometric enhancement and standardization; (c) output binary segmentation mask generated by the U-Net; and (d) qualitative validation depicting the predicted roller contours superimposed onto the rectified image. 13

3 Training and validation convergence curves of the U-Net model adapted from Sáez et al. (2026). Top row: local fine-tuning performance at the Maipo River site, showing (a.1) Binary Cross Entropy loss function and (a.2) F1-Score evolution across epochs for the specialized Wave Breaking Detection (WBD) model compared against a generic Transfer Learning (TL) baseline. The shaded area indicates the onset of overfitting identified beyond epoch 10. Bottom row (b.1, b.2): corresponding benchmark curves for the Saint-Pierre (France) reference site. 14

4 **Conceptual framework for mapping 2D planar U-Net masks to wave-breaking energy dissipation.** (a) Top-view optical footprint derived from the U-Net binary mask $M(x, y, t)$, identifying the local wave propagation angle (α), beach orientation (β), and cross-shore roller width (L_r). (b) Vertical cross-sectional reconstruction of the turbulent roller wedge following Duncan (1981). The projected width L_r and wave face slope $\theta \approx 15°$ reconstruct the vertical area $A_r = 0.11(L_r/\cos\theta)^2$. Line dissipation ($D_L$) is converted into planar instantaneous dissipation (D_{inst}) via slice-wise orthogonal projection and scaled to sea-state phase-averaged dissipation (D_{br}) via the pixel temporal occupancy fraction. 15

5 **Schematic representation of the spatiotemporal tracking algorithm for phase celerity (C) and wave propagation angle (θ_{az}).** The binary mask at frame t (blue) and translated frame $t + \Delta t$ (red) are fitted with equivalent ellipses using second-order spatial moments. The major axis represents the strong axis (longitudinal wave crest), while the orthogonal minor axis defines the weak axis (primary propagation direction). Net physical advance (Δd) is measured along the weak axis vector from centroid C_t to its geometric intersection point (P_{int}) with the strong axis at $t + \Delta t$. Phase celerity is computed as $C = \Delta d/\Delta t$. Propagation direction is converted to a True North-referenced azimuth angle (θ_{az}). 20

6 The DJI Air 3 Unmanned Aerial Vehicle (UAV) employed for the high-resolution optical surveys at the Maipo River mouth. Image courtesy of DJI. 21

7 **Spatially resolved wave kinematics, energy dissipation, and hydrodynamic roller forcing under high-energy oblique swell conditions (Scenario 1: 24 March 2025, $H_s = 1.71\,\mathbf{m}$, $T_p = 12.80\,\mathbf{s}$, $\theta_p = 296.8°$).** (a) Spatial distribution of wave phase celerity (c). (b) Wave propagation directions referenced to True North (θ_{az}), highlighting topography-induced wave refraction over the outer sandbar. (c) Sea-state time-averaged breaking energy dissipation (D_{br}). (d) Hydrodynamic forcing vector field ($\mathbf{F}_r$) demonstrating notable alongshore momentum components. All fields are uniformly masked for $X < 250\,\mathrm{m}$ to isolate outer-to-intermediate surf zone processes from inner swash interference. 23

8 **Spatially resolved wave kinematics, energy dissipation, and hydrodynamic roller forcing under high-energy shore-normal swell conditions (Scenario 2: 17 December 2025, $H_s = 1.71\,\mathbf{m}$, $T_p = 10.24\,\mathbf{s}$, $\theta_p = 271.6°$).** (a) Spatial distribution of wave phase celerity (c) with a strict threshold at $X < 100\,\mathrm{m}$. (b) Discrete block-averaged wave propagation azimuths referenced to True North (θ_{az}) with color scale constrained to 180°–360°. (c) Sea-state time-averaged breaking energy dissipation (D_{br}). (d) Hydrodynamic forcing vector field ($\mathbf{F}_r$) showing predominantly cross-shore momentum thrust towards the shore. 25

9 **Benchmarking of observed vs. theoretical shallow-water wave celerity ($C_{\mathrm{th}} = \sqrt{g \cdot h}$) across both evaluated scenarios.** (a) High-energy oblique swell on 24 March 2025 (Scenario 1: $H_s = 1.71\,\mathrm{m}$, $T_p = 12.80\,\mathrm{s}$, $\theta_p = 296.8°$), capturing a broad kinematic range and slight non-linearities (RMSE = $0.97\,\mathrm{m/s}$, $R^2 = 0.685$). (b) High-energy shore-normal swell on 17 December 2025 (Scenario 2: $H_s = 1.71\,\mathrm{m}$, $T_p = 10.24\,\mathrm{s}$, $\theta_p = 271.6°$), which exhibits the largest observation volume ($N = 132,289$) and a steeper scaling trend (best-fit $y = 1.28x - 0.94$, $R^2 = 0.729$), with increased scatter (RMSE = $1.44\,\mathrm{m/s}$) influenced by complex wave-discharge interactions near the active estuarine mouth. The dashed orange line represents the upper kinematic filter limit ($2 \cdot C_{\mathrm{th}}$) applied to isolate unphysical tracking errors. 31

10 **Non-linear hydrodynamic coupling between roller area (A_r), breaking fraction (Q_b), and mean wave roller dissipation ($\bar{D}_{\mathrm{inst}}$) for the March 2025 survey ($H_s = 1.71\,\mathbf{m}$, $T_p = 12.80\,\mathbf{s}$).** 34

11 **Non-linear hydrodynamic coupling between roller area (A_r), breaking fraction (Q_b), and mean wave roller dissipation ($\bar{D}_{\mathrm{inst}}$) for the December 2025 survey ($H_s = 1.71\,\mathbf{m}$, $T_p = 10.24\,\mathbf{s}$).** 35

12 Spatial correlation matrices representing the interdependencies between hydrodynamic variables for the March 2025 event ($H_s = 1.71$ m, $T_p = 12.80$ s). The 6×6 matrices evaluate wave celerity (c), phase-averaged dissipation (D_{br}), direction (θ_{az}), roller force (F_r), roller area footprint (A_r), and the wave breaking fraction (Q_b). (a) Pearson correlation matrix (r). (b) Spearman rank correlation matrix (ρ). 36

13 Spatial correlation matrices representing the interdependencies between hydrodynamic variables for the December 2025 event ($H_s = 1.71$ m, $T_p = 10.24$ s). The matrices evaluate wave celerity (c), phase-averaged dissipation (D_{br}), direction (θ_{az}), roller force (F_r), roller area footprint (A_r), and the wave breaking fraction (Q_b). (a) Pearson correlation matrix (r). (b) Spearman rank correlation matrix (ρ). 37

14 Exact log-variance decomposition and partial correlations for phase-averaged dissipation (D_{br}) and roller force (F_r) during the March 2025 long-period swell event. . . . 38

15 Exact log-variance decomposition and partial correlations for phase-averaged dissipation (D_{br}) and roller force (F_r) during the December 2025 steep wave event. 39

List of Tables

1 Summary of UAV survey schedules and concurrent offshore hydrodynamic conditions recorded by the Port of San Antonio ADCP. 22
2 Comparative trade-off matrix: UAV-based optical image processing vs. process-based numerical modeling for surf zone hydrodynamics. 42

1. INTRODUCTION

Wave forcing acts as a primary driver of coastal morphodynamics, dictating the evolution and behavior of shorelines across a wide range of spatial and temporal scales (Castelle & Masselink, 2022; Ranasinghe, 2016). As incident waves propagate into shallow waters and break, the resulting energy dissipation drives nearshore currents and momentum fluxes that continuously redistribute sediments, shaping features such as sandbars, berms, and broader shoreline configurations (Coco et al., 2014; Wright & Short, 1984). Within this dynamic zone, the physical force exerted by the wave roller—the aerated turbulent fluid mass advancing along the front face of a breaking wave—acts as the primary mechanism transferring momentum into the underlying water column and driving nearshore circulation. Consequently, a comprehensive understanding and spatially resolved characterization of wave-dominated processes, breaking dissipation, and roller-induced forcing is essential for evaluating sediment budgets, predicting shoreline response to extreme events, and developing robust coastal protection and management strategies (Toimil et al., 2017).

While wave forcing drives general open-coast dynamics, river mouths constitute exceptionally complex and critical transition zones where energetic wave climates directly interact with freshwater discharges. This fluviomarine interplay generates intricate hydrodynamic patterns that govern local sediment transport, spit breaching, and estuarine bar formation (Besset et al., 2019; Liu et al., 2024). Beyond their physical complexity, these estuarine environments foster highly productive ecosystems that regulate water quality, act as natural sediment filters, and shelter diverse biological communities (Barbier et al., 2011; Galbán-Malagón et al., 2023; Gómez et al., 2021). Preserving these zones and ensuring the safety of adjacent anthropogenic settlements requires an accurate understanding of the coupled flow mechanics (Spalding et al., 2014). The Maipo River mouth in central Chile exemplifies such a dynamic environment, having recently experienced severe morphodynamic anomalies, including river mouth closure and extreme localized flooding (Martínez & Saldías, 2023). Because active estuarine discharge channels induce sharp horizontal velocity shears, wave blocking, and rapid bathymetric changes, elucidating the dominant wave-breaking mechanics at this site serves as an ideal and challenging testbed for nearshore hydrodynamic frameworks.

However, characterizing wave breaking and quantifying wave-induced momentum fluxes in energetic river-wave interaction zones remains a major scientific and operational challenge (Feddersen et al., 2016; Roco et al., 2024; Rodriguez et al., 2018). This difficulty arises largely because conventional measurement tools are often insufficient to capture the highly non-linear and chaotic nature of surf-zone fluid mechanics (Perlin et al., 2013). In-situ deployments, such as acoustic Doppler current profilers (ADCPs) and pressure transducer arrays, provide high-fidelity point measurements (Feddersen, 2014; Flores et al., 2016); nevertheless, the destructive surf-zone environment makes their deployment risky, expensive, and spatially sparse, failing to resolve the high-frequency spatial heterogeneity of the breaking field. To circumvent these observational gaps, process-based numerical models (e.g., SWAN, XBeach, COAWST) have become the operational standard for resolving nearshore hydrodynamics (Olabarrieta et al., 2005, 2011; Rojas et al., 2023; Warner et al., 2010). Yet, the diagnostic accuracy of these models is fundamentally constrained by their acute sensitivity to bathymetric boundary conditions. In dynamic estuarine environments, morphological changes occur on time scales of hours to days during high-energy events, often rendering bathymetric inputs obsolete before a simulation can even be executed. Furthermore, numerical estimations of wave dissipation rely on phase-averaged, depth-limited breaking parameterizations (e.g., the γ breaking criterion) tuned to bulk offshore parameters, which frequently fail to capture transient surf-zone physics, localized diffraction, and wave-current shear (Roelvink et al., 2009). Therefore, a critical problem remains unresolved: how to accurately, continuously, and non-intrusively quantify spatially

distributed wave forcing in dynamic coastal environments without relying on constantly updated bathymetric surveys.

Remote sensing has emerged as a compelling, non-intrusive alternative to overcome these observational bottlenecks (Almar et al., 2012; Díez et al., 1999). Early optical methodologies evolved from time-exposure photography (Timex) for sandbar mapping (Holman & Stanley, 2007) to pixel-intensity thresholding for breaking detection. However, simple brightness-based heuristics are inherently vulnerable to environmental contamination, generating false positives from persistent remnant foam and false negatives under cloud shadows or water glint. To enhance detection, remote sensing applications progressed toward statistical formulations, such as probability density functions derived from video and radar records to segment breaking crests from passive foam (Catalán et al., 2011). More recently, data-driven machine learning architectures have superseded heuristic approaches: shallow neural networks were first applied to predict wave breaking fractions (Stringari et al., 2019), while Convolutional Neural Networks (CNNs) were developed to classify breaker types from aerial imagery (Buscombe & Carini, 2019). The latest advances harness deep learning semantic segmentation architectures—specifically U-Net models—which achieve pixel-level precision by learning multi-scale spatial hierarchies and textural context rather than absolute grayscale brightness (Sáez et al., 2021, 2026). Parallel to these computational developments, experimental fluid mechanics has formalized the physical link between surface breaker geometry and hydrodynamics. Controlled laboratory flume experiments have demonstrated how roller momentum governs flow accelerations (Xue et al., 2023), while recent studies have established empirical formulations linking roller cross-sectional geometry to wave energy dissipation (Wu et al., 2025). Furthermore, coherent X-band Doppler radar has shown the feasibility of diagnosing surf-zone dissipation directly from surface velocities (Grossmann et al., 2026).

These combined technological and theoretical milestones present an unexploited opportunity to bridge computer vision with fundamental fluid mechanics. Rather than deploying neural networks solely for qualitative breaker detection, deep learning can be operationalized as an observational hydrodynamic tool. Crucially, resolving nearshore circulation requires a paradigm shift: extracting wave forcing directly from the surface physical manifestation of the breaking roller, rather than inferring it from bottom-up bathymetric depth equations.

To address this challenge, this study introduces a non-intrusive observational framework that integrates high-resolution Unmanned Aerial Vehicle (UAV) video imagery, deep learning semantic segmentation (U-Net), and spatiotemporal kinematic tracking to continuously diagnose surf-zone hydrodynamic forcing and energy dissipation. By retrieving the geometric roller footprint, tracking phase celerity, and resolving local wave-number vectors directly from surface optical footprints, the proposed pipeline solves the wave momentum flux balance observationally. This approach provides distinct operational advantages: it eliminates the vulnerability to bathymetric obsolescence that compromises numerical models, naturally discriminates active breakers across optically complex estuarine plumes, and delivers spatially continuous 2D vector fields of dissipation and forcing. The methodology is tested and validated using field surveys collected across contrasting wave climates at the Maipo River mouth (Chile), establishing a robust, observation-driven foundation for nearshore hydrodynamic monitoring, depth inversion, and coastal hazard assessment.

2. OBJECTIVES AND HYPOTHESES

Quantifying wave-induced forcing and energy dissipation in dynamic river-wave interaction zones is essential for assessing coastal morphodynamics. However, traditional observational approaches and process-based numerical models are fundamentally constrained by hazardous surf zone conditions and a critical reliance on rapidly outdated bathymetry. To overcome these bottlenecks, the overarching purpose of this research is to develop, validate, and apply a non-intrusive observational framework that integrates Unmanned Aerial Vehicle (UAV) imagery, deep learning semantic segmentation (U-Net), and spatiotemporal kinematic tracking to continuously resolve surf zone hydrodynamic forcing directly from surface optical footprints. By targeting the characteristic spatial morphology of active breaking rollers across optically complex estuarine backgrounds, this methodology establishes a robust, observation-driven paradigm that isolates wave-by-wave instantaneous mechanics from sea-state phase-averaged dissipation, enabling the quantification of coastal momentum fluxes without the need for continuously updated bathymetric boundary conditions.

2.1 General Objective

To determine and quantitatively validate surf zone hydrodynamic forcing (F_r) and phase-averaged wave breaking dissipation (D_{br}) using a deep learning-enhanced UAV remote sensing framework, evaluating the influence of contrasting incident wave climates on the physical coupling between turbulent roller geometry (A_r), stochastic breaking intermittency (Q_b), and kinematic phase celerity (c) at a dynamic river mouth.

2.2 Specific Objectives

1. **Deep Learning Semantic Segmentation:** To implement and locally fine-tune a U-Net convolutional neural network architecture capable of accurately isolating active wave rollers from complex optical backgrounds, mitigating false detections typically induced by sediment-laden estuarine plumes and persistent remnant foam.

2. **High-Resolution Kinematic Extraction:** To develop a spatiotemporal tracking algorithm based on image moments that extracts wave phase celerity (c) and propagation direction (θ_{az}) directly from segmented optical footprints, utilizing static baseline bathymetry solely for establishing physical upper-bound tracking thresholds to circumvent the need for real-time bathymetric updates.

3. **Hydrodynamic Dissipation and Forcing Computation:** To map 2D planar roller footprints to 3D vertical cross-sectional areas using an orthogonal strip-theory formulation, enabling the dimensionally consistent computation of instantaneous dissipation, phase-averaged energy dissipation (D_{br}), and the spatial divergence of roller-induced momentum fluxes ($\vec{F}_r$) based on Duncan's energy-balance mechanics.

4. **Cross-Regime Multivariate Decoupling:** To statistically disentangle the physical drivers of nearshore wave forcing under contrasting wave climates (long-period spilling swell versus steep, short-period plunging waves) using exact log-variance decomposition and partial correlations, isolating the direct thermodynamic contribution of the roller footprint from bathymetrically induced spatial covariances.

2.3 Hypotheses

- **Methodological Hypothesis:** Deep learning semantic segmentation (U-Net) can successfully decouple the physical signature of active breaking rollers from background optical noise and estuarine plumes. By continuously retrieving roller geometry and kinematic celerity directly from these surface optical signatures, wave momentum flux and hydrodynamic forcing can be robustly diagnosed, effectively circumventing the reliance on continuously updated bathymetric data required by standard process-based numerical models.

- **Physical Hypothesis:** In the surf zone hydrodynamic momentum balance, the planar geometric footprint of the wave roller (A_r) acts as a direct physical determinant of mechanical energy dissipation (D_{br}) across all wave climates, including steep plunging regimes, provided that the stochastic spatial intermittency of wave breaking (Q_b) is statistically controlled. Simultaneously, wave phase celerity (c) operates universally as a kinematic momentum attenuator, reducing the local momentum flux density by constraining the temporal residence of the roller over the underlying water column.

3. METHODOLOGY

3.1 Roller Force Estimation

In the depth-averaged vorticity balance, the contribution of the irrotational wave radiation stress terms becomes negligible in non-divergent shallow flows, leaving the curl of the roller-induced force—representing the spatial gradient of energy flux dissipated within the surf zone—as the primary driver of rotational circulation and rip currents. Conversely, in the momentum balance, radiation stress gradients remain significant because the wave field continuously transports and redistributes momentum prior to and during breaking (Longuet-Higgins & Stewart, 1964). Consequently, the total wave-induced forcing can be conceptualized as the superposition of the roller-mediated momentum transfer and the gradients associated with the remaining organized wave motion, reflecting the distinct physical roles of individual wave-energy components in driving the coastal mean flow.

The present formulation focuses specifically on the roller-induced hydrodynamic force, derived from the coupled wave energy and momentum balances within the surf zone (Stive & de Vriend, 1994; Svendsen, 1984). To maintain strict dimensional and physical consistency, three distinct hydrodynamic quantities must be separated: (i) the wave-roller pseudo-momentum density $\mathbf{M}_r = (E_r/c)\mathbf{n}$ [$\mathrm{N \cdot s/m^2}$], representing momentum per unit horizontal surface area, where E_r is the roller energy density [$\mathrm{J/m^2}$] and $\mathbf{n} = \mathbf{k}/|\mathbf{k}|$ is the unit vector pointing in the direction of wave propagation; (ii) the vertically integrated roller momentum flux tensor, or roller radiation stress $\mathbf{S}_r$ [N/m]; and (iii) the net hydrodynamic force per unit horizontal surface area transferred to the underlying water column, $\vec{F}_r$ [$\mathrm{N/m^2}$], which is governed by the negative divergence of this momentum flux:

$$\vec{F}_r = -\nabla \cdot \mathbf{S}_r \tag{1}$$

Under stationary or phase-averaged breaking conditions, the divergence of the organized energy flux is balanced by breaking-induced dissipation ($-D_{br}$, with D_{br} in $\mathrm{W/m^2}$). Because wave momentum flux scales directly with energy flux divided by phase speed ($c = \omega/|\mathbf{k}|$) (Phillips, 1977), the spatial gradient of radiation stress induced by turbulent dissipation scales with D_{br}/c (Chen et al., 2024). Projecting along the local wave-number vector yields Equation 2:

$$\vec{F}_r = \frac{D_{br}}{c}\frac{\vec{k}}{|\vec{k}|} = \frac{D_{br}}{c}\hat{k} \tag{2}$$

This formulation explicitly incorporates the unit wave-number vector $\hat{k}$, enabling the simultaneous quantification of both the magnitude and spatial orientation of the hydrodynamic forcing exerted across the surf zone and the estuarine plume front. It couples spatial estimates of breaking-induced energy dissipation (D_{br}) with the local phase speed (c), both fundamental for parameterizing wave-driven flow accelerations. Dimensional consistency is strictly preserved: dividing the surface energy dissipation rate ([$\mathrm{W/m^2}$] $\equiv$ [$\mathrm{N \cdot m/(s \cdot m^2)}$]) by the phase celerity ([m/s]) yields units of [$\mathrm{N/m^2}$]. This corresponds to a horizontal surface shear stress (or force per unit area) in the momentum equations, directly parameterizing the momentum transfer from aerated breaking rollers into the mean flow.

While Feddersen et al. (2016) successfully implemented this physical balance within a coupled numerical framework (ROMS-SWAN), process-based numerical models rely heavily on accurate, up-to-date bathymetric inputs and empirical breaking criteria (e.g., γ-based formulations) to diagnose dissipation and forcing fields. In dynamic estuarine environments such as the Maipo River mouth, where morphodynamic modifications occur rapidly on tidal-to-event scales and strong current shears

modulate breaking mechanics, numerical models frequently misplace the spatial locus and intensity of the breaking front. In contrast, the present study solves Equation 2 observationally. By diagnosing D_{br}, c, and $\hat{k}$ directly from surface optical footprints via the UAV pipeline detailed in Sections 3.2–3.4, a spatially continuous vector field of wave forcing is reconstructed based on the actual physical manifestation of the breaking process (Figure 1). This approach decouples forcing estimation from real-time bathymetric tracking, providing a direct, observation-driven characterization of the hydrodynamic drivers acting across the estuarine outflow.

The proposed automated pipeline (Figure 1) is structured around a computer-vision algorithm designed to retrieve wave roller kinematics, spatial forcing, and energy dissipation from high-resolution video sequences. The workflow initiates by extracting geometric descriptors—namely cross-sectional areas, principal axes, and centroids—from the binary roller masks segmented by the U-Net, complemented by offshore wave climate and baseline morphodynamic parameters. To track individual wave rollers across successive frames, the algorithm optimizes inter-frame centroid displacements to derive the measured roller celerity (C_m). To ensure physical consistency and eliminate tracking artifacts, each empirical celerity is evaluated against a theoretical upper-bound threshold (C_{th}), derived from shallow-water Linear Wave Theory (LWT) scaled by representative baseline depths and slopes. If C_m satisfies the physical constraint ($C_m \leq C_{th}$), the algorithm logs the roller identifier and kinematics, sequentially triggering the energy dissipation module. In this step, orthogonal transects are sampled across the segmented roller footprints to apply Duncan's geometric formulation (Duncan, 1981); the resulting instantaneous dissipation rates are accumulated and phase-averaged onto orthogonal spatial grids. Conversely, if C_m exceeds C_{th}, the roller is flagged as collapsed or dissipated, prompting an alternate directional assessment via its weak principal axis before advancing to subsequent wave features.

3.2 Data Curation

The primary dataset comprises high-frequency optical imagery collected from Unmanned Aerial Vehicle (UAV) video surveys. To prepare raw optical sequences for deep learning segmentation and subsequent kinematic analysis, a structured workflow was implemented, distinguishing between mandatory photogrammetric corrections and flexible, dataset-dependent formatting steps. As an essential standard requirement for quantitative optical oceanography, raw oblique frames were geometrically orthorectified into a planar, top-view (2D) horizontal projection using photogrammetric calibration procedures (Bruder & Brodie, 2020). Following orthorectification, dataset-dependent spatial adjustments—such as frame rotation to align the alongshore/cross-shore axes—can be selectively applied depending on the orientation of the survey. Furthermore, to match the input tensor specifications (512×512 pixels) of the U-Net architecture (Sáez et al., 2026), target imagery can be formatted either via spatial cropping, uniform resizing, or a combination of both, tailored to the specific field of view, spatial extent, and native resolution of the acquisition system. In this study, rectified frames were converted to grayscale to reduce computational dimensionality and rescaled to the 512×512 tensor size while preserving critical nearshore wave dynamics. Finally, to enable the physical interpretation of wave kinematics and energy dissipation, a rigorous spatial calibration factor (meters-per-pixel conversion) was established directly on the post-formatted imagery using georeferenced ground control points in QGIS (QGIS Development Team, 2024), ensuring that all derivative fields are evaluated in true physical metrics.

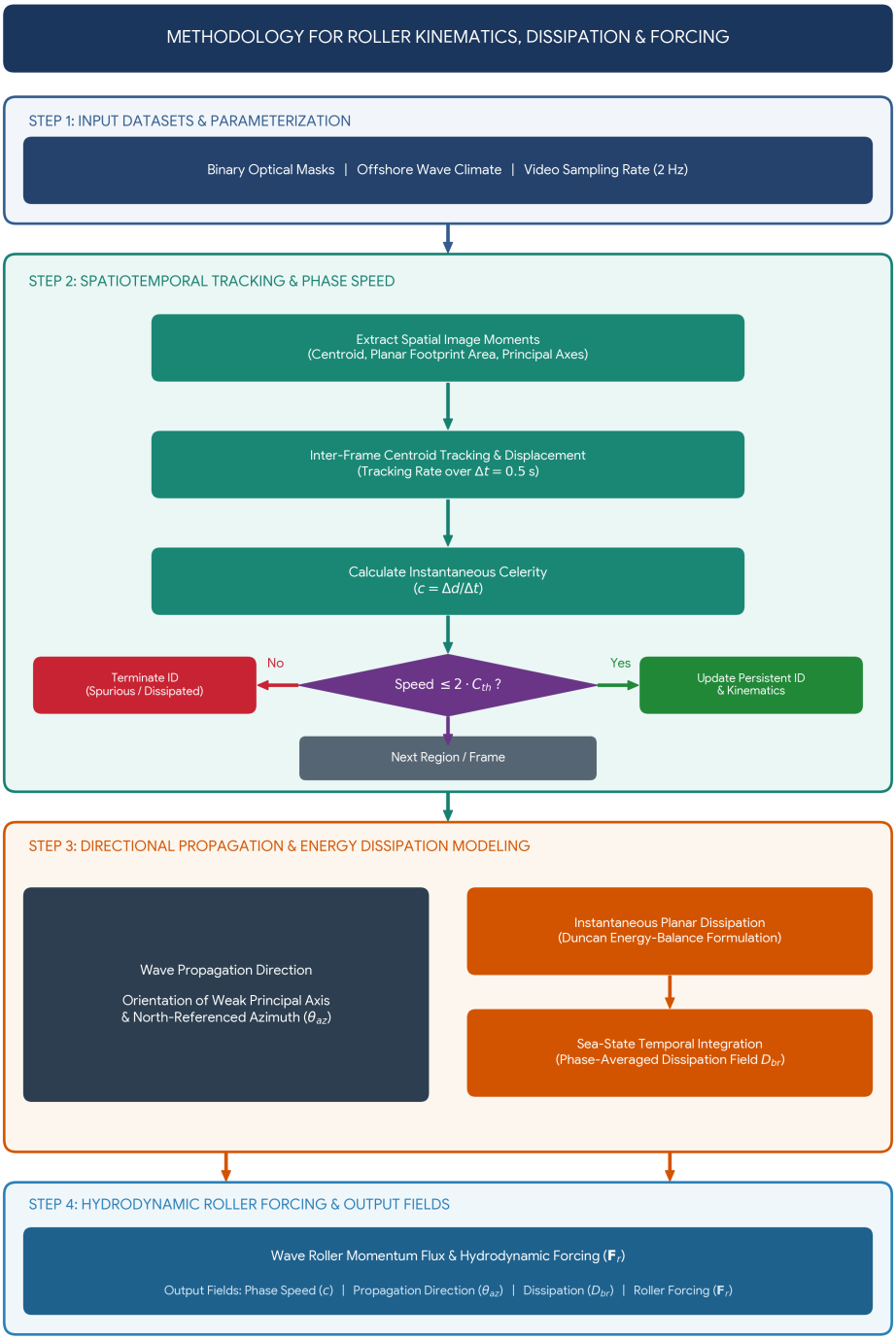
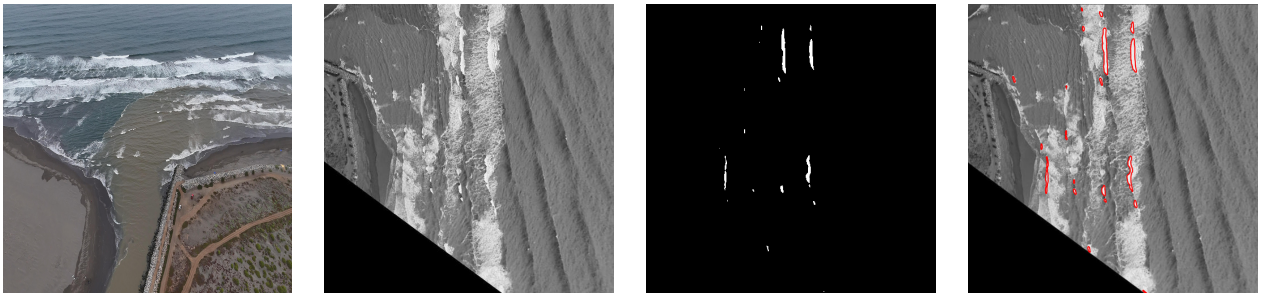


Figure 1: Flowchart of the automated methodology for estimating breaking wave roller force and energy dissipation. The algorithmic structure comprises three main modules: continuous roller tracking and celerity estimation (green), wave propagation direction assessment for dissipated rollers (grey), and spatial energy dissipation computation applying Duncan's formulation (orange). Tracking fidelity is governed by a physical control filter that compares the measured centroid celerity (C_m) against a theoretical threshold (C_{th}) derived from Linear Wave Theory.

3.3 Wave breaking detection

Addressing the observational bottlenecks highlighted previously, a deep learning approach based on the U-Net architecture detailed by Sáez et al. (2021) and Sáez et al. (2026) was employed to automate the identification of active breaking regions. This Convolutional Neural Network (CNN) is designed for semantic segmentation, assigning a discrete class label to every pixel in the input image. In this study, the network output is defined as a binary mask—a pixel-wise classification matrix where a value of 1 corresponds to active breaking wave rollers and 0 represents the background (non-breaking water, sandbar deposits, or dry beach) (Fig. 2).



(a) Raw UAV (b) Data Curation (c) Binary Mask (d) Superimposed

Figure 2: Sequential visualization of the proposed image processing pipeline: (a) raw RGB aerial frame; (b) radiometric enhancement and standardization; (c) output binary segmentation mask generated by the U-Net; and (d) qualitative validation depicting the predicted roller contours superimposed onto the rectified image.

Figure 2 illustrates the sequential image processing workflow implemented in this study. The pipeline begins with raw RGB imagery acquired by the UAV (panel a). The frame then undergoes geometric rectification, radiometric enhancement, and spatial filtering as detailed in the *Data Curation* section to maximize feature extractability, yielding the standardized input image (panel b). Panel (c) displays the binary mask produced by the U-Net segmentation. Finally, panel (d) shows the extracted roller boundaries superimposed onto the preprocessed image, confirming the geometric fidelity of the detected turbulent fronts.

To adapt the base architecture to the distinct optical signatures of the study site, the network underwent local post-training refinement (fine-tuning) utilizing representative video footage collected at the Maipo River mouth (Sáez et al., 2026), which encompassed conditions representative of the March 2025 survey. Fine-tuning the network locally is critical in fluviomarine transition zones, where severe optical contamination—such as high turbidity, suspended sediment discharge, and lingering remnant foam—frequently leads to catastrophic failure in conventional thresholding algorithms.

The training and validation trajectories documented by Sáez et al. (2026) (Fig. 3) demonstrate the effectiveness of this localized learning process. For the Maipo River site (Fig. 3a.1, a.2), the specialized Wave Breaking Detection (WBD) network demonstrates superior convergence compared to standard transfer learning (TL). The Binary Cross Entropy (BCE) loss function for the WBD model decreases rapidly and stabilizes at very low values ($\sim$ 0.03–0.04) on both training and validation sets (Fig. 3a.1). Concurrently, the F1-Score rises sharply, reaching an optimal plateau of $\sim$ 0.78 on the training set and stabilizing between 0.70 and 0.72 on the validation cohort within the first 8 to 10 epochs (Fig. 3a.2). Beyond epoch 10, the validation loss begins to diverge slightly while validation F1-Scores plateau, defining the operational early-stopping boundary to prevent overfitting. These metrics confirm that the network successfully learned the contextual, spatial-textural features of

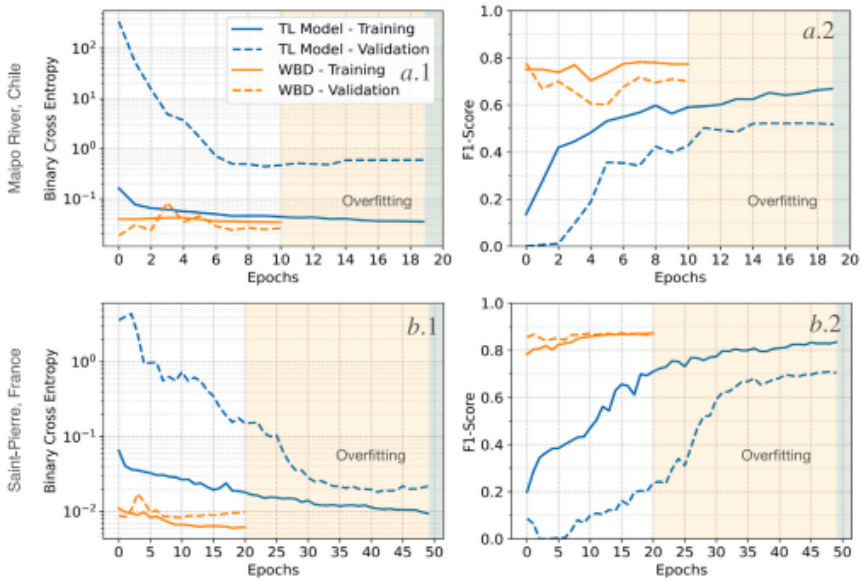


Figure 3: Training and validation convergence curves of the U-Net model adapted from Sáez et al. (2026). Top row: local fine-tuning performance at the Maipo River site, showing (a.1) Binary Cross Entropy loss function and (a.2) F1-Score evolution across epochs for the specialized Wave Breaking Detection (WBD) model compared against a generic Transfer Learning (TL) baseline. The shaded area indicates the onset of overfitting identified beyond epoch 10. Bottom row (b.1, b.2): corresponding benchmark curves for the Saint-Pierre (France) reference site.

active breaking foam while learning to reject sediment-laden estuarine plumes and quiescent water surfaces.

Crucially, while the model benefited from local post-training refinement on datasets encompassing conditions representative of the March 2025 campaign, the December 2025 survey was held out entirely as an unseen, out-of-sample benchmark. The network received no additional training, calibration, or fine-tuning on the December 2025 footage. The stable convergence achieved during local refinement provided the robust feature representations necessary to reliably segment this unseen dataset, despite marked changes in wave steepness, plunging breaker dynamics, and estuarine outflow geometry. The resulting binary masks thus establish a reliable, physically sound foundation for subsequent wave tracking, kinematic extraction, and hydrodynamic energy dissipation modeling.

3.4 Energy Dissipation by Wave Breaking Estimation

The aerated surface roller accounts for the dominant fraction of turbulent kinetic energy dissipated across the surf zone, making its physical parameterization essential for quantifying nearshore momentum transfer and wave-driven circulation (Chen et al., 2024; Stive & de Vriend, 1994; Svendsen, 1984). Duncan (1981) established a classical momentum- and energy-balance formulation for quasi-steady spilling breakers generated by a towed hydrofoil. In this framework, the aerated roller is idealized as a turbulent fluid wedge sliding down the sloping forward face of the wave at angle θ relative to the horizontal. The downward component of the gravitational force acting on the fluid wedge along the sloping interface is balanced by the turbulent shear stress ($\bar{\tau}$) exerted at the lower roller boundary of length L. Integrating the tangential momentum equation yields the net shear force per unit crest length (F_τ [N/m]):

$$F_\tau = \bar{\tau} L = \rho g A_r \sin(\theta) \tag{3}$$

where ρ is the seawater density ($\approx 1025\,\mathrm{kg/m^3}$), g is the acceleration due to gravity, A_r is the vertical cross-sectional area of the roller [$\mathrm{m^2}$], and θ is the inclination angle of the wave face.

Crucially, the dimensionless prefactor 0.11 established by Duncan (1981) does not represent an empirical force-scale factor; rather, it reflects a geometric self-similarity relationship governing the vertical cross-sectional area of steady spilling rollers:

$$A_r = 0.11\, L^2 \tag{4}$$

where L is the roller length measured along the sloping wave face. Preserving this single physical origin of the 0.11 coefficient prevents the double application that arises if the factor is simultaneously embedded within the force balance and the cross-sectional area parameterization.

The rate of mechanical energy dissipated per unit crest length (D_L [W/m $\equiv$ N/s]) corresponds to the work performed by this boundary shear force per unit time as the wave propagates at phase speed c:

$$D_L = F_\tau \cdot c = \rho g A_r c \sin(\theta) \tag{5}$$

establishing exact dimensional consistency ([N/m] $\cdot$ [m/s] = [W/m]).

3.4.1 Rigorous Mapping from 2D Planar Footprints to Instantaneous Dissipation

A primary operational challenge in optical remote sensing lies in retrieving the vertical cross-sectional area A_r from monocular, two-dimensional planar video that records only the horizontal projection of the breaker. To bridge this geometric dimensionality, the binary segmentation mask $M(x, y, t) \in \{0, 1\}$ extracted by the U-Net architecture is linked to the vertical wedge geometry using an orthogonal strip-theory slicing scheme, as illustrated in Figure 4.

Figure 4: **Conceptual framework for mapping 2D planar U-Net masks to wave-breaking energy dissipation.** (a) Top-view optical footprint derived from the U-Net binary mask $M(x, y, t)$, identifying the local wave propagation angle (α), beach orientation (β), and cross-shore roller width (L_r). (b) Vertical cross-sectional reconstruction of the turbulent roller wedge following Duncan (1981). The projected width L_r and wave face slope $\theta \approx 15^\circ$ reconstruct the vertical area $A_r = 0.11(L_r/\cos\theta)^2$. Line dissipation ($D_L$) is converted into planar instantaneous dissipation (D_{inst}) via slice-wise orthogonal projection and scaled to sea-state phase-averaged dissipation (D_{br}) via the pixel temporal occupancy fraction.

To operationalize this mapping across natural breakers with non-uniform crest dimensions, the optical footprint is discretized into orthogonal transects oriented parallel to the local wave propagation vector $\hat{k}$. By virtue of the roller's large aspect ratio ($L_r \ll L_{\mathrm{crest}}$), cross-shore spatial gradients of free-surface elevation and momentum flux strongly dominate over along-crest variations ($\partial/\partial y \ll \partial/\partial x$). Consequently, lateral turbulent momentum exchange between adjacent strips is of secondary order, allowing each orthogonal transect s to be modeled as an independent, quasi-2D hydrodynamic strip governed locally by its cross-shore chord width $L_r(s)$. Along each transect, the conversion follows a sequential kinematic and geometric reconstruction:

- **Local Cross-Shore Chord Width ($L_r(s)$):** Along each orthogonal transect s, the distance between the leading and trailing edges of the binary mask defines the local cross-shore roller chord length, $L_r(s)$ [m]. By sampling L_r slice-by-slice, the algorithm explicitly accounts for along-crest width variability rather than imposing a single spatially uniform average.

- **Vertical Cross-Sectional Area ($A_r(s)$):** From wave-front trigonometry, the sloping boundary length $L(s)$ along the breaker face relates to the planar chord width via $L(s) = L_r(s)/\cos(\theta)$. Substituting this expression into Duncan's geometric relation (Eq. 4) yields the vertical area for transect s:

$$A_r(s) = 0.11 \left(\frac{L_r(s)}{\cos(\theta)} \right)^2 = 0.11 \frac{L_r^2(s)}{\cos^2(\theta)} \tag{6}$$

- **Phase Celerity (c):** The local propagation speed $c(x, y, t)$ [m/s] is obtained from the inter-frame spatiotemporal tracking of roller centroids along the propagation direction ($c = \Delta d/\Delta t$), as detailed in Section 3.5.

- **Wave Face Angle Parameterization (θ):** In planar monocular imagery without stereoscopic topography, θ must be parameterized from coastal hydrodynamic principles. In oceanic surf zones, while the initial jet impact in plunging breakers can exhibit localized inclinations exceeding 25°, the forward face of actively breaking and spilling rollers rapidly stabilizes into a quasi-steady regime bounded between 12° and 18° (Duncan, 1981; Schäffer et al., 1993). Following canonical surf-zone roller formulations (Díaz et al., 2018; Svendsen, 1984), a representative value of $\theta = 15°$ is selected.

Substituting the geometric reconstruction of $A_r(s)$ (Eq. 6) into the dissipation rate per unit crest length (Eq. 5) yields the instantaneous energy dissipation rate for that specific transect ($D_L(s)$, [W/m]):

$$D_L(s) = 0.11\, \rho g L_r^2(s) c \frac{\sin(\theta)}{\cos^2(\theta)} = 0.11\, \rho g L_r^2(s) c \frac{\tan(\theta)}{\cos(\theta)} \tag{7}$$

To transform this line dissipation rate into a spatially continuous planar instantaneous dissipation field ($D_{\text{inst}}(x, y, t)$, [W/m^2]), the mechanical dissipation across strip s is distributed over its corresponding cross-shore chord $L_r(s)$. Assuming a top-hat cross-shore energy distribution across the active roller footprint—a standard first-order approximation in the absence of continuous 3D free-surface profile measurements—the planar dissipation at each breaking pixel $(x, y) \in$ strip s is evaluated as:

$$D_{\text{inst}}(x, y, t) = \frac{D_L(s)}{L_r(s)} = 0.11\, \rho g L_r(s) c(x, y, t) \frac{\tan(\theta)}{\cos(\theta)} \quad \text{for } M(x, y, t) = 1 \tag{8}$$

with $D_{\text{inst}}(x, y, t) = 0$ for quiescent, non-breaking pixels where $M(x, y, t) = 0$.

This orthogonal strip-theory formulation provides a mathematically consistent bridge between 1D laboratory dissipation mechanics and 2D planar imagery. First, it explicitly accommodates longitudinal variations in roller thickness along the wave front by evaluating $L_r(s)$ locally along each orthogonal transect. Second, it maintains strict energy flux conservation: integrating $D_{\text{inst}}(x, y, t)$ across the cross-shore chord length $\int_0^{L_r(s)} D_{\text{inst}}\, \mathrm{d}x$ exactly recovers the linear dissipation rate $D_L(s)$. Finally, the geometric coefficient 0.11 enters solely through the vertical area parameterization A_r, eliminating artificial empirical scalings and ensuring full dimensional consistency ([W/m^2]). Evaluating the geometric sensitivity across the full range $\theta \in [12°, 18°]$ reveals that $f(\theta) = \tan(\theta)/\cos(\theta)$

increases moderately from 0.217 to 0.342—a bounded factor of ~ 1.57, in contrast to the spurious factor of ~ 2.34 introduced by $\tan^2(\theta)$ dependencies in earlier heuristic studies. Adopting the canonical baseline $\theta = 15^\circ$ ($f(15^\circ) = 0.277$) entails a maximum parametric uncertainty of $\pm 23\%$ across the entire morphological breaker spectrum, confirming that the order of magnitude of D_{inst} is dynamically constrained.

3.4.2 Distinction Between Pixel Occupancy and Sea-State Breaking Fraction

While $D_{\text{inst}}(x, y, t)$ quantifies high-frequency energetic bursts during the transient passage of individual breaking crests, spectral wave action models (e.g., SWAN (Booij et al., 1999)) and nearshore circulation schemes compute the steady energy dissipation rate averaged over entire sea states and wave cycles (D_{br} [W/m^2]) (Battjes & Janssen, 1978).

To bridge high-frequency optical observations with continuum coastal formulations, the video record is discretized into N_{total} sampled frames acquired at a sampling frequency $f_s = 1/\Delta t = 2\,\text{Hz}$ over a total observation duration $T_{\text{total}} \approx 30\,\text{min}$ ($N_{\text{total}} = 3600$). From a physical perspective, the phase-averaged sea-state dissipation corresponds to the continuous time integral of instantaneous mechanical power per unit horizontal area:

$$D_{br}(x, y) = \frac{1}{T_{\text{total}}} \int_0^{T_{\text{total}}} D_{\text{inst}}(x, y, t)\, \mathrm{d}t \approx \frac{1}{N_{\text{total}} \Delta t} \sum_{k=1}^{N_{\text{total}}} D_{\text{inst}}(x, y, k)\, \Delta t = \frac{1}{N_{\text{total}}} \sum_{k=1}^{N_{\text{total}}} D_{\text{inst}}(x, y, k) \tag{9}$$

Crucially, the exact algebraic cancellation of the sampling step Δt ensures that Eq. (9) represents a consistent discrete Riemann sum that is intrinsically invariant to video frame rate. Because an active roller possesses a finite cross-shore width (L_r) and propagates at a finite phase speed (c), its physical transit over a fixed spatial coordinate spans a non-zero residence time:

$$\tau_r(x, y) \approx \frac{L_r(x, y)}{c(x, y)} \tag{10}$$

When $\tau_r > \Delta t$ (for instance, a roller of $L_r \approx 3\,\text{m}$ advancing at $c \approx 3\,\text{m/s}$ requires $\tau_r \approx 1.0\,\text{s}$, thereby intersecting the same pixel across two consecutive frames at 2 Hz), the algorithm registers non-zero instantaneous dissipation across both frames. This multi-frame persistence is not an artifact of double-counting; rather, it reflects the physical duration over which turbulent shear stress continuously performs mechanical work on that water column. Higher sampling frequencies merely discretize this continuous work with finer temporal resolution without inflating the resulting time-averaged dissipation.

From this discrete formulation, Eq. (9) can be decomposed into the conditional mean dissipation during active breaking events, $\bar{D}_{\text{active}}(x, y)$, and the temporal pixel occupancy fraction, $f_{\text{occ}}(x, y)$:

$$D_{br}(x, y) = \bar{D}_{\text{active}}(x, y) \cdot f_{\text{occ}}(x, y) \tag{11}$$

where the pixel occupancy fraction is defined directly from the segmented binary sequence:

$$f_{\text{occ}}(x, y) = \frac{N_{\text{active}}(x, y)}{N_{\text{total}}} = \frac{T_{\text{active}}(x, y)}{T_{\text{total}}} \tag{12}$$

A fundamental physical distinction must be drawn between this image-derived pixel occupancy fraction $f_{\text{occ}}(x, y)$ and the classic wave-by-wave breaking fraction $Q_b(x, y)$ defined in statistical

wave theory (Battjes & Janssen, 1978; Thornton & Guza, 1983). The parameter $Q_b(x,y) = N_{\text{break}}(x,y)/N_{\text{waves}}$ represents the fraction of individual waves within the sea state that undergo breaking at position (x,y), where the total number of passing waves over the survey duration is governed by the offshore peak wave period T_p:

$$N_{\text{waves}} \approx \frac{T_{\text{total}}}{T_p} \tag{13}$$

The total duration of active roller presence over a pixel during the video survey corresponds to the product of the number of independent breaking waves and their single-event residence time: $T_{\text{active}}(x,y) = N_{\text{break}}(x,y) \cdot \tau_r(x,y)$. Substituting this expression into Eq. (12) establishes the analytical relationship linking optical pixel occupancy to the statistical wave breaking fraction and peak period T_p:

$$f_{\text{occ}}(x,y) = \frac{N_{\text{break}}(x,y)\,\tau_r(x,y)}{(T_{\text{total}}/T_p)\,T_p} = \left(\frac{N_{\text{break}}(x,y)}{N_{\text{waves}}}\right)\left(\frac{\tau_r(x,y)}{T_p}\right) = Q_b(x,y)\left(\frac{L_r(x,y)}{c(x,y)T_p}\right) \tag{14}$$

Equation (14) proves that $f_{\text{occ}}(x,y)$ equals the wave breaking fraction $Q_b(x,y)$ scaled by the roller duty cycle, $\tau_r(x,y)/T_p = L_r(x,y)/\lambda(x,y)$, where $\lambda(x,y) = c(x,y)T_p$ is the local shallow-water wavelength. Consequently, integrating Eq. (9) through continuous frame averaging accounts for both the spatial breaking probability (Q_b) and roller residence intermittency (τ_r/T_p), scaling localized crest dissipation peaks ($\sim 10^3\,\text{W/m}^2$) down to sea-state phase-averaged values ($D_{br} \sim 10^2\,\text{W/m}^2$) in rigorous agreement with continuum wave modeling (Catalán & Haller, 2008; Díaz et al., 2018).

This transformation from instantaneous dissipation (D_{inst}) to phase-averaged dissipation (D_{br}) is physically and numerically essential for nearshore hydrodynamic modeling. While Duncan's (Duncan, 1981) formulation provides an accurate description of instantaneous turbulent work during active crest transit, relying directly on D_{inst} to evaluate wave forcing ($\vec{F}_r$) is ill-suited for resolving mean coastal circulation. In natural random wave fields, active rollers exhibit strong spatiotemporal intermittency, generating short-lived, localized bursts of dissipation ($\sim 10^3\,\text{W/m}^2$) followed by quiescent intervals ($D_{\text{inst}} = 0$). Directly injecting these high-frequency impulsive stresses into phase-averaged circulation models (e.g., ROMS, Delft3D, or stationary 2DH momentum balances) introduces artificial velocity spikes, numerical instabilities, and fails to represent the quasi-steady radiation stress gradients that physically govern mean water level setup, undertow, and rip current dynamics. By scaling the optical measurements into a continuous, phase-averaged metric ($D_{br} \sim 10^2\,\text{W/m}^2$) equivalent to spectral wave formulations (Battjes & Janssen, 1978; Booij et al., 1999), the framework filters out wave-group intermittency and crest-level stochasticity. This provides a direct, dimensionally compatible bridge for coupling remote-sensing observations with continuum coastal hydrodynamic models, enabling rigorous benchmark comparisons against SWAN dissipation fields and establishing a stable surface forcing field representative of the governing sea state.

3.5 Kinematic Characterization: Celerity and Propagation Direction

To retrieve the kinematic properties required for Equation 2, the binary masks generated by the U-Net are processed using the OpenCV library (Bradski, 2000). This step involves computing the spatial image moments for each segmented region, yielding critical geometric descriptors including the surface area, centroid coordinates, and principal orientation axes.

For the estimation of phase celerity (C), a spatiotemporal tracking algorithm is implemented

based on the geometric evolution of the roller contours. Initially, a unique identifier (ID) is assigned to each detected region. Across consecutive frames, a Nearest Neighbor approach propagates these IDs by associating candidate centroids subject to a multivariate kinematic and directional filter. First, an upper velocity threshold is established based on the local theoretical shallow-water wave speed ($C_{\text{th}} = \sqrt{g \cdot h}$) derived from Linear Wave Theory (LWT) (Dean & Dalrymple, 1991). To define a robust upper tracking envelope, a scaling factor of 2 is applied to this theoretical baseline ($2 \cdot C_{\text{th}} = 2\sqrt{g \cdot h}$), establishing the maximum allowable inter-frame displacement. This factor of 2 provides a conservative margin that accommodates highly non-linear, finite-amplitude wave propagation and high-momentum transients (Lippmann & Holman, 1991; Svendsen, 1984) while strictly preventing unphysical centroid leaps across distinct wave fronts. Detected regions exceeding this upper displacement threshold are classified as newly initiated breaking events rather than continuations, thereby mitigating misidentification errors due to spatial overlap or wave dissipation. Second, a directional progression constraint is enforced, based on the physical requirement that breaking rollers propagate irreversibly forward along the dominant wave propagation trajectory. Because active rollers cannot travel backward, candidates that exhibit a negative displacement component along the local propagation direction (i.e., retrograding or moving in reverse relative to the forward-advancing wave propagation vector $\vec{k}/\|\vec{k}\|$) are immediately rejected. This ensures that only forward-moving, onshore-advancing centroids are tracked, preventing erroneous association with older remnant foam or misidentified backward-moving pixels. Third, a lower velocity threshold is enforced to discard all celerities below 1 m/s. This constraint is physically grounded in the need to filter out the wave runup and swash zone near the shoreline; in this shallow margin, the slow, oscillatory movement of foam over the beach face no longer complies with the hydrodynamics and geometric assumptions of an active breaking roller, instead representing swash-zone runup processes that must be excluded from the surf-zone celerity dataset.

Once a roller contour is successfully tracked across consecutive frames, its phase celerity is quantified using its principal geometric axes derived from second-order central moments, as schematically illustrated in Figure 5. Specifically, the orientation of the equivalent fitted ellipse is decomposed into its major (strong) axis, which aligns with the longitudinal crest of the roller, and its orthogonal minor (weak) axis, which defines the primary direction of wave propagation. To determine the net physical advance, the effective displacement (Δd) is measured along the vector of the weak principal axis from the initial centroid position (C_t) to its geometric intersection (P_{int}) with the strong principal axis of the translated roller at $t+\Delta t$ (Fig. 5). Phase celerity (C) is then obtained by dividing this directional displacement by the frame sampling interval ($\Delta t = 1/\text{FPS}$). This orthogonal projection framework provides a robust physical foundation that effectively accommodates wave refraction and dynamically shifting propagation angles over complex bathymetry, while simultaneously preventing speed misestimations caused by unconstrained centroid drift or asymmetrical roller deformation.

Simultaneously, the wave propagation direction is resolved to define the unit vector $\frac{\vec{k}}{\|\vec{k}\|}$ required for the forcing formulation. To ensure consistency with oceanographic standards, the directional angles derived from the weak principal axis are transformed into a North-referenced azimuth system (0° corresponding to True North), following the conventions established in the Coastal Engineering Manual (US Army Corps of Engineers, 2002). Rather than deriving a single bulk direction or applying a linear arithmetic mean—which fails across the 0°/360° branch-cut discontinuity—the orientation vectors are spatially aggregated using circular (directional) statistics (Mardia & Jupp, 2000). Within each regular spatial grid cell (25×25 pixels), the mean wave propagation direction $\bar{\theta}$ is derived from the first circular trigonometric moments:

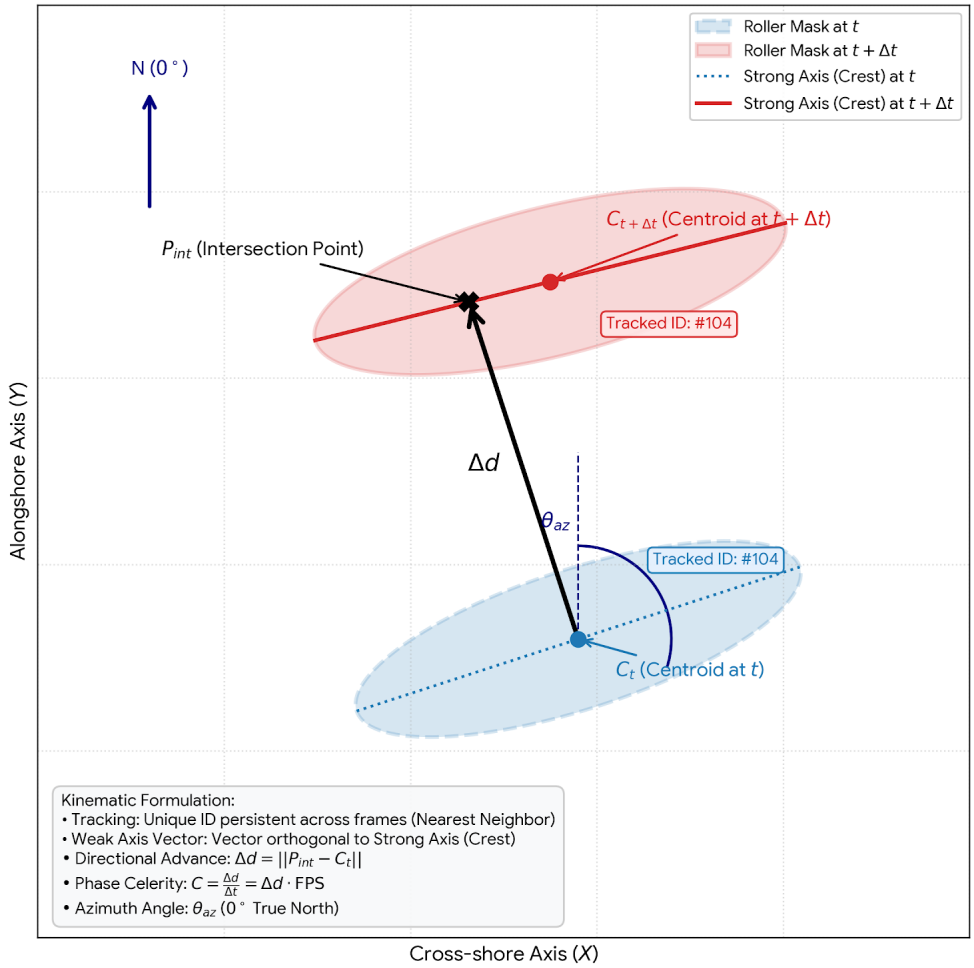


Figure 5: **Schematic representation of the spatiotemporal tracking algorithm for phase celerity (C) and wave propagation angle (θ_{az}).** The binary mask at frame t (blue) and translated frame $t + \Delta t$ (red) are fitted with equivalent ellipses using second-order spatial moments. The major axis represents the strong axis (longitudinal wave crest), while the orthogonal minor axis defines the weak axis (primary propagation direction). Net physical advance (Δd) is measured along the weak axis vector from centroid C_t to its geometric intersection point (P_{int}) with the strong axis at $t + \Delta t$. Phase celerity is computed as $C = \Delta d / \Delta t$. Propagation direction is converted to a True North-referenced azimuth angle (θ_{az}).

$$\bar{\theta} = \text{atan2}\left(\bar{S}, \bar{C}\right), \quad \text{with} \quad \bar{S} = \frac{1}{N}\sum_{i=1}^{N}\sin(\theta_i), \quad \bar{C} = \frac{1}{N}\sum_{i=1}^{N}\cos(\theta_i) \tag{15}$$

where N is the number of valid wave orientation samples within the cell, and θ_i represents the instantaneous local propagation angle. To assess directional spreading and filtering uncertainty within each bin, the mean resultant vector length $\bar{R} \in [0, 1]$ and the corresponding circular variance S_0 are defined as:

$$\bar{R} = \sqrt{\bar{S}^2 + \bar{C}^2}, \quad S_0 = 1 - \bar{R} \tag{16}$$

where $\bar{R} \to 1$ indicates near-perfect directional alignment (unidirectional wave propagation), while $\bar{R} \to 0$ characterizes extreme directional spreading or chaotic turbulent motions. Cells exhibiting high angular dispersion ($\bar{R} < 0.70$) or insufficient tracking samples are flagged as unorganized motions and discarded. This circular formulation generates a spatially resolved, continuous vector field of wave directions that accurately captures refraction, shoaling rotation, and diffraction patterns across the surf zone without angular wrapping distortions.

4. STUDY CASES

The proposed image-processing workflow was evaluated using field data acquired at the Maipo River mouth in Santo Domingo, Chile. A series of aerial surveys were conducted using a DJI Air 3 Unmanned Aerial Vehicle (UAV) (Fig. 6), equipped with a dual-camera system capable of capturing 48-megapixel still images and 4K video at 60 fps (10-bit D-Log M color profile). To ensure robust testing across contrasting environmental conditions, two distinct field campaigns were executed in March 2025 and December 2025. From the raw continuous footage of each flight, frames were subsampled at a frequency of 2 Hz to yield sequences of high-resolution images, which were subsequently processed following the methodology described in Section 2.



Figure 6: The DJI Air 3 Unmanned Aerial Vehicle (UAV) employed for the high-resolution optical surveys at the Maipo River mouth. Image courtesy of DJI.

To characterize the hydrodynamic conditions during the surveys, concurrent offshore wave parameters were extracted from an Acoustic Doppler Current Profiler (ADCP) deployed at the Port of San Antonio (Empresa Portuaria San Antonio, n.d.). The specific schedules for each UAV flight and the corresponding significant wave height (H_s), peak period (T_p), and peak wave direction (θ_p) are summarized in Table 1. Crucially, both campaigns captured identical offshore energy levels in

terms of significant wave height ($H_s = 1.71\,\mathrm{m}$), but differed substantially in spectral peak period ($T_p = 12.80\,\mathrm{s}$ vs. $10.24\,\mathrm{s}$) and approach direction ($\theta_p = 296.8°$ vs. $271.6°$). This setup provides a controlled empirical framework to isolate the influence of wave steepness and wave-group periodicity on surf zone dynamics. Given that wave breaking properties—such as roller geometry and kinematics—have been shown to be highly sea-state dependent (Guimarães et al., 2026), documenting these offshore conditions is critical to support a robust physical interpretation of the remotely derived estimates of celerity, dissipation, and roller dynamics across both survey dates.

Table 1: Summary of UAV survey schedules and concurrent offshore hydrodynamic conditions recorded by the Port of San Antonio ADCP.

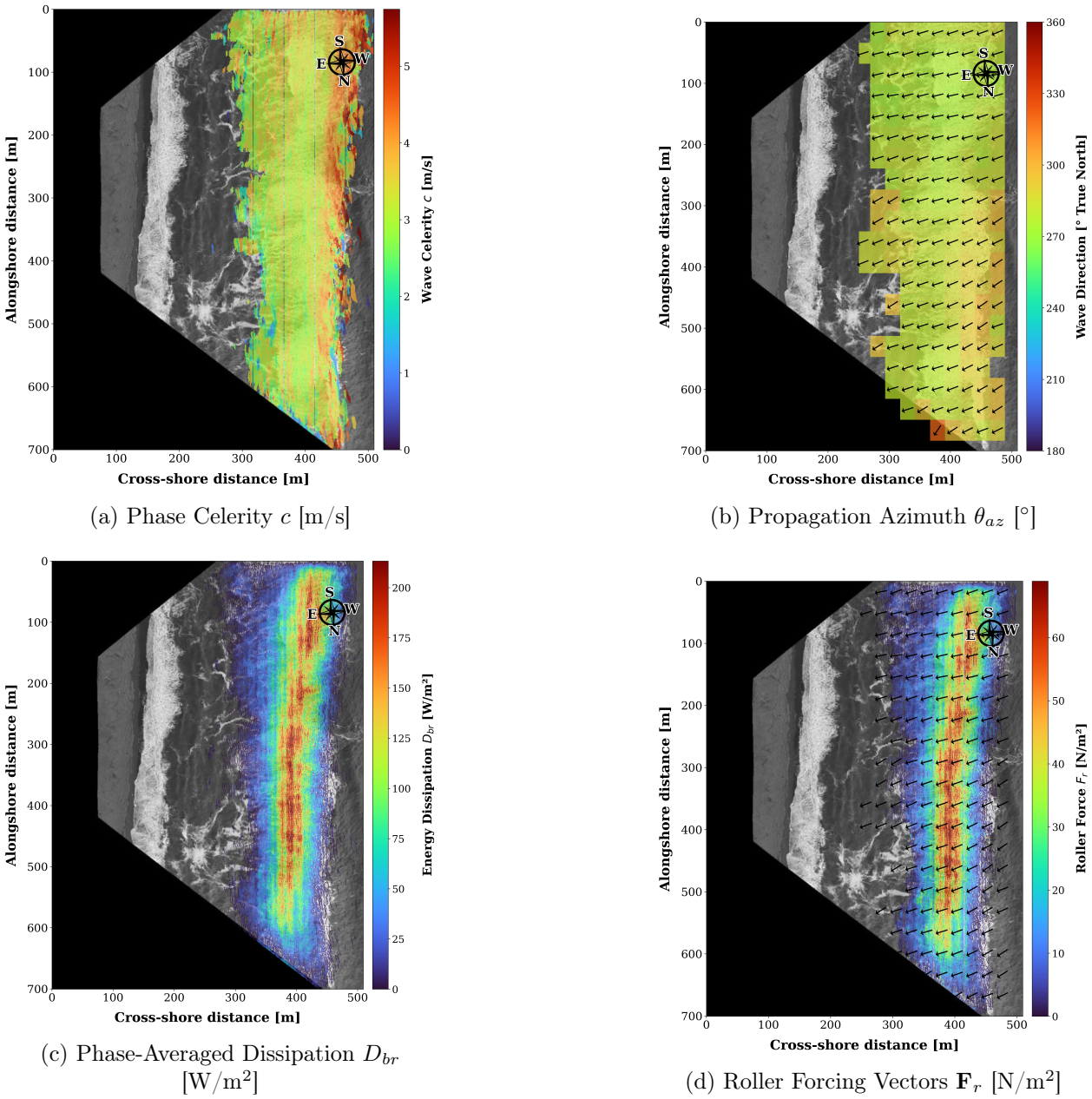
Date	**Local Time**	H_s **(m)**	T_p **(s)**	θ_p **(°)**
24 March 2025	15:07:35 – 15:32:36	1.71	12.80	296.8
17 December 2025	15:08:54 – 15:39:04	1.71	10.24	271.6

Baseline bathymetric characteristics were derived from official hydrographic charts provided by the Hydrographic and Oceanographic Service of the Chilean Navy (SHOA, Chart No. 5111, *"Bahía de San Antonio y Proximidades"*, scale 1:20,000; Edition 2021). The bathymetric sounding data are georeferenced to the horizontal datum WGS-84 (Projected Coordinate System UTM Zone 19S) and vertically reduced to the Chart Datum (CD, *Nivel de Reducción de Sondas*—NRS), which closely corresponds to the Lowest Astronomical Tide (LAT). For computational processing, the discrete soundings and digitized isobaths were interpolated onto a regular spatial grid with a resolution of 10×10 m.

Regarding temporal correspondence, while the baseline hydrographic survey predates the UAV flight campaigns (March 2025 and December 2025), cross-shore transects extracted across the nearshore domain confirm a uniform, low-sloping seabed characterized by a representative mean beach slope of 1.4% ($\tan\beta \approx 0.014$). Crucially, within the presented observational framework, this bathymetric dataset is not utilized as a dynamic input to compute wave energy fluxes, depth inversion, or wave dissipation. Instead, its operational utility is strictly confined to two static calibration roles: (i) defining the representative domain slope ($\tan\beta$) for geometric roller parametrization, and (ii) establishing conservative, shallow-water upper-bound celerity thresholds ($C_{th} = 1.3\sqrt{gh}$) to filter spurious tracking artifacts in the kinematic module. Consequently, the temporal decoupling between the historical bathymetric baseline and the instantaneous UAV surveys does not induce cumulative errors in the retrieved dissipation and roller force fields, as both quantities are diagnosed directly from instantaneous surface optical signatures.

5. RESULTS

5.1 Scenario 1: High-Energy Oblique Swell ($H_s = 1.71\,\mathbf{m}$, $T_p = 12.80\,\mathbf{s}$, $\theta_p = 296.8°$)



(a) Phase Celerity c [m/s]

(b) Propagation Azimuth θ_{az} [°]

(c) Phase-Averaged Dissipation D_{br} [W/m^2]

(d) Roller Forcing Vectors $\mathbf{F}_r$ [N/m^2]

Figure 7: **Spatially resolved wave kinematics, energy dissipation, and hydrodynamic roller forcing under high-energy oblique swell conditions (Scenario 1: 24 March 2025, $H_s = 1.71\,\mathbf{m}$, $T_p = 12.80\,\mathbf{s}$, $\theta_p = 296.8°$).** (a) Spatial distribution of wave phase celerity (c). (b) Wave propagation directions referenced to True North (θ_{az}), highlighting topography-induced wave refraction over the outer sandbar. (c) Sea-state time-averaged breaking energy dissipation (D_{br}). (d) Hydrodynamic forcing vector field ($\mathbf{F}_r$) demonstrating notable alongshore momentum components. All fields are uniformly masked for $X < 250\,\mathrm{m}$ to isolate outer-to-intermediate surf zone processes from inner swash interference.

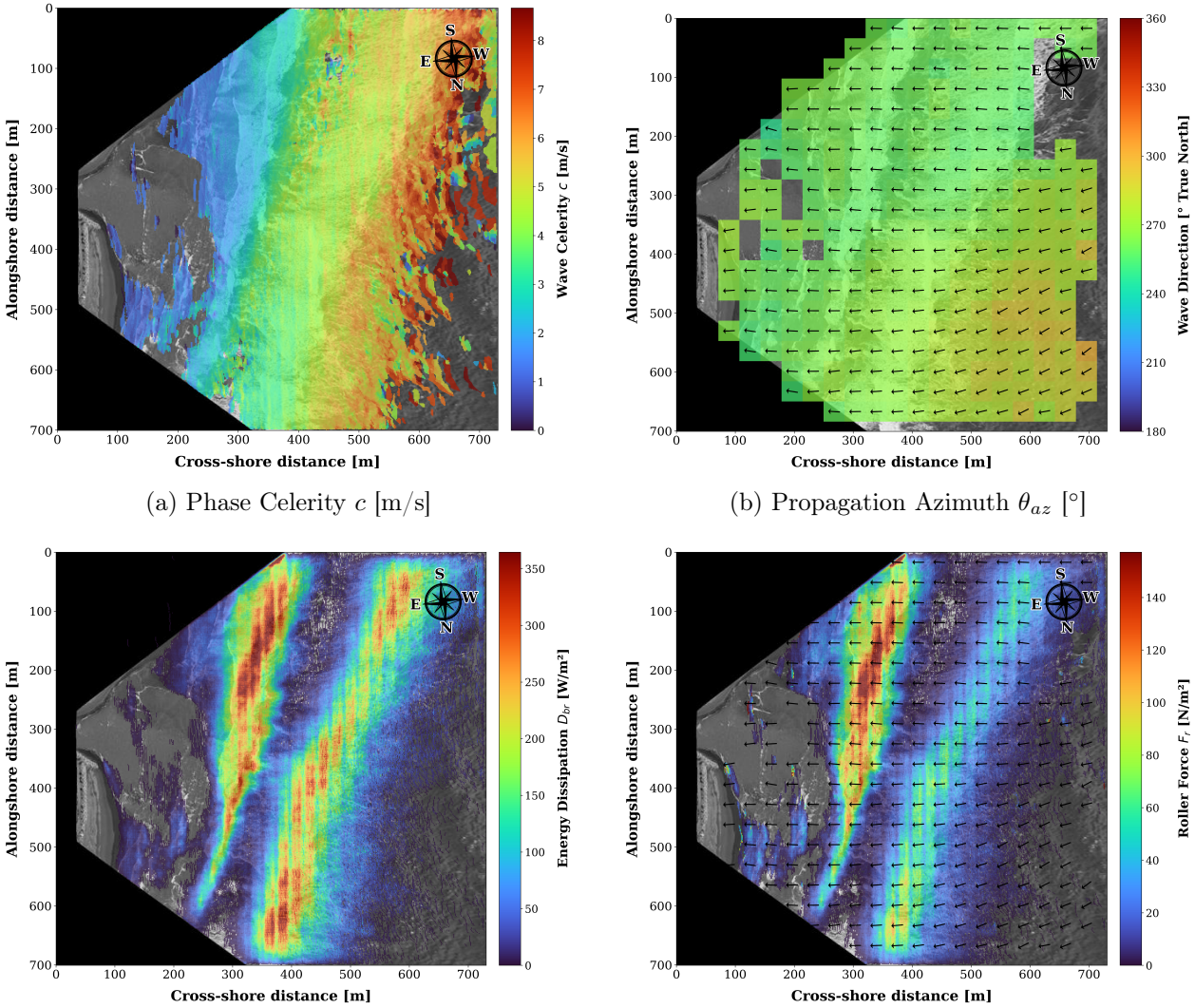
Under the energetic, oblique swell conditions of Scenario 1 ($H_s = 1.71\,\mathrm{m}$, $T_p = 12.80\,\mathrm{s}$, $\theta_p = 296.8°$), the hydrodynamic fields are resolved across the outer and intermediate surf zone domain ($X \geq 250\,\mathrm{m}$ up to $X \approx 500\,\mathrm{m}$), with a homogeneous spatial filter applied for $X < 250\,\mathrm{m}$ to exclude nearshore swash noise and unbreaking inner zones. Within this active window, the wave phase celerity field (Fig. 7a) displays a pronounced depth-limited shoaling deceleration. Seaward velocities attain maximum values between 4.5 and 5.8 m/s in the offshore region ($X > 430\,\mathrm{m}$), progressively slowing to intermediate speeds of 3.0–4.2 m/s across the seaward bar slope ($X = 350$–$430\,\mathrm{m}$), and decreasing to 1.8–2.8 m/s near the inner resolved threshold ($X = 250$–$320\,\mathrm{m}$).

Concurrently, the block-averaged wave propagation direction map (Fig. 7b) captures the topographically driven refraction across the bar. In the outer domain ($X > 420\,\mathrm{m}$), the incident wave field exhibits an oblique orientation with propagation azimuths ranging between $\theta_{az} \approx 290°$ and 305°. As wave fronts propagate across the bathymetric slopes of the outer sandbar ($X = 260$–$400\,\mathrm{m}$), depth-induced refraction rotates the crests toward a more shore-normal alignment ($\theta_{az} \approx 270°$–$285°$), with the vector arrows pointing predominantly westward prior to reaching the inner cutoff boundary.

The phase-averaged energy dissipation map (Fig. 7c) resolves a continuous, coast-parallel breaking band focused over the outer sandbar ($X = 360$–$440\,\mathrm{m}$, spanning alongshore from $Y = 50\,\mathrm{m}$ to $650\,\mathrm{m}$), with values ranging from 0 to $215\,\mathrm{W/m^2}$. Under this long-period swell state ($T_p = 12.80\,\mathrm{s}$), primary wave breaking is concentrated along this outer bar deposit, where turbulent energy dissipation peaks between 175 and $215\,\mathrm{W/m^2}$. Both seaward of the bar crest ($X > 460\,\mathrm{m}$) and shoreward into the intermediate trough ($X < 330\,\mathrm{m}$), dissipation drops sharply below $25\,\mathrm{W/m^2}$, indicating wave re-formation over the deeper trough prior to entering the masked nearshore domain.

Finally, the hydrodynamic roller force density (Fig. 7d) exhibits values up to 68–70 $\mathrm{N/m^2}$, tightly replicating the spatial morphology of the dissipation field across the outer bar ($X = 360$–$440\,\mathrm{m}$). Peak force magnitudes (50–68 $\mathrm{N/m^2}$) are concentrated along the primary breaking line. Due to the oblique swell approach, the resulting forcing vector field ($\mathbf{F}_r$) contains significant alongshore force components oriented southward alongside the cross-shore onshore thrust, providing the key hydrodynamic momentum input necessary to drive alongshore current circulation and sediment transport along the outer sandbar.

5.2 Scenario 2: High-Energy Shore-Normal Swell ($H_s = 1.71\,\mathbf{m}$, $T_p = 10.24\,\mathbf{s}$, $\theta_p = 271.6°$)



(a) Phase Celerity c [m/s]

(b) Propagation Azimuth θ_{az} [°]

(c) Phase-Averaged Dissipation D_{br} [W/m^2]

(d) Roller Forcing Vectors $\mathbf{F}_r$ [N/m^2]

Figure 8: **Spatially resolved wave kinematics, energy dissipation, and hydrodynamic roller forcing under high-energy shore-normal swell conditions (Scenario 2: 17 December 2025, $H_s = 1.71\,\mathbf{m}$, $T_p = 10.24\,\mathbf{s}$, $\theta_p = 271.6°$).** (a) Spatial distribution of wave phase celerity (c) with a strict threshold at $X < 100\,\mathrm{m}$. (b) Discrete block-averaged wave propagation azimuths referenced to True North (θ_{az}) with color scale constrained to 180°–360°. (c) Sea-state time-averaged breaking energy dissipation (D_{br}). (d) Hydrodynamic forcing vector field ($\mathbf{F}_r$) showing predominantly cross-shore momentum thrust towards the shore.

Under the energetic, shore-normal swell conditions of Scenario 2 ($H_s = 1.71\,\mathrm{m}$, $T_p = 10.24\,\mathrm{s}$, $\theta_p = 271.6°$), the phase celerity field (Fig. 8a) spans a wide cross-shore extent up to $X = 750\,\mathrm{m}$. Wave propagation speeds exhibit a continuous, bathymetrically controlled deceleration, decreasing from maximum offshore values (6.5–8.5 m/s at $X > 550\,\mathrm{m}$) through intermediate speeds (3.5–6.0 m/s

across $X = 300$–$550\,\mathrm{m}$), down to less than $2.5\,\mathrm{m/s}$ in the shallow nearshore region ($100\,\mathrm{m} \leq X \leq 250\,\mathrm{m}$). A strict threshold masks out regions with $X < 100\,\mathrm{m}$ across all hydrodynamic fields to eliminate dry beach or highly non-linear swash noise.

Concurrently, the discrete grid-block directional map (Fig. 8b) reflects the nearly shore-normal approach of the offshore swell within a constrained color scale (180°–360°). Because the incident wave orientation ($\theta_p = 271.6°$) is almost orthogonal to the coastal bathymetric contours, minimal spatial refraction occurs across the domain. Propagation azimuths remain highly uniform ($\theta_{az} \approx 265°$–$275°$), with the vector arrows pointing almost strictly westward toward the coastline.

The phase-averaged dissipation map (Fig. 8c) displays two well-defined, coast-parallel breaking bands extending across the domain ($Y = 50$–$650\,\mathrm{m}$), with values ranging from 0 to $360\,\mathrm{W/m^2}$. An outer breaking zone over the seaward sandbar ($X = 380$–$520\,\mathrm{m}$) accounts for substantial preliminary energy loss (150–$280\,\mathrm{W/m^2}$). Shoreward of this bar, waves re-form across an intermediate trough before undergoing intense secondary breaking along the inner bar ($X = 180$–$300\,\mathrm{m}$), where dissipation reaches peak values of 300–$360\,\mathrm{W/m^2}$. Notably, the morphodynamic influence of the river mouth is resolved in the inner zone ($X < 220\,\mathrm{m}$, $Y = 300$–$450\,\mathrm{m}$), where bathymetric deepening caused by the estuarine discharge channel inhibits depth-limited breaking, producing a localized gap of near-zero dissipation.

Finally, the hydrodynamic roller forcing density (Fig. 8d) reaches up to $150\,\mathrm{N/m^2}$, with peak magnitudes (110–$150\,\mathrm{N/m^2}$) tightly aligned with the inner breaking bar ($X = 180$–$300\,\mathrm{m}$). In contrast to oblique swell cases, the shore-normal wave incidence generates forcing vectors ($\mathbf{F}_r$) oriented almost exclusively in the cross-shore direction. This direct onshore momentum flux acts primarily as a perpendicular thrust driving wave setup and cross-shore mass transport toward the beach face and estuarine mouth rather than driving alongshore currents.

5.3 Cross-Scenario Hydrodynamic Synthesis

A comparative analysis between both evaluated hydrodynamic scenarios demonstrates the capacity of the proposed UAV-deep learning framework to resolve complex, variable nearshore processes driven by offshore wave climate and localized morphodynamics. Because both campaigns share an identical significant wave height ($H_s = 1.71\,\mathrm{m}$; Table 1), this comparative synthesis provides a controlled baseline that isolates the governing roles of wave period ($T_p = 12.80\,\mathrm{s}$ vs. $10.24\,\mathrm{s}$), wave steepness (H_s/L_0), and incident wave direction ($\theta_p = 296.8°$ vs. $271.6°$) on the resulting spatial fields of phase celerity (c), energy dissipation (D_{br}), and roller forcing ($\mathbf{F}_r$).

5.3.1 Wave Climate Control and Dissipation Dynamics

While significant wave height dictates the overall seaward boundary of the surf zone ($X > 400$–$550\,\mathrm{m}$ in both events), the spatial structure and cross-shore partitioning of energy dissipation (D_{br}) are strongly controlled by wave period and steepness. In Scenario 1 ($T_p = 12.80\,\mathrm{s}$), the long-period, organized swell undergoes progressive spilling dissipation that is primarily concentrated over the outer sandbar ($X = 350$–$450\,\mathrm{m}$), reaching peak values of 175–$210\,\mathrm{W/m^2}$. Waves subsequently re-form across the deeper intermediate trough without developing a major secondary breaking zone. Conversely, in Scenario 2 ($T_p = 10.24\,\mathrm{s}$), the steeper wave climate generates a pronounced bimodal dissipation structure: an outer breaking band over the seaward bar ($X = 380$–$520\,\mathrm{m}$, 150–$280\,\mathrm{W/m^2}$) is followed by severe secondary plunging breaking over the shallow inner bar ($X = 180$–$300\,\mathrm{m}$), where dissipation reaches peak values of 300–$360\,\mathrm{W/m^2}$.

5.3.2 Bar Structural Variability and the Role of the River Mouth Channel

The spatial continuity of active breaking zones reflects immediate coupling with underlying morphodynamic features:

- **Single-Bar vs. Bimodal Dissipation Structure:** Under long-period swell (Scenario 1), energy decay is largely localized over the outer sandbar, which serves as a hydrodynamic buffer dissipating the bulk of incident wave power. Under shorter-period, steeper waves (Scenario 2), residual wave energy penetrates across the trough and triggers a violent inner breaker zone, concentrating turbulent kinetic energy within 200 m of the shoreline.
- **Estuarine Outflow Filtering:** The presence of the river mouth discharge channel introduces a critical spatial asymmetry, clearly resolved in Scenario 2. While intense secondary breaking occurs over the shallow inner bar ($X = 180$–300 m), dissipation drops abruptly to near-zero values within the deeper estuarine outflow channel ($X < 220$ m, $Y = 300$–450 m). The increased water depth within the discharge channel suppresses depth-limited breaking, allowing unruptured wave energy to propagate further into the estuarine entrance. The framework accurately identifies this bathymetric gap without generating false-positive breaking detections, proving its robustness in complex estuarine-coastal transition zones.

5.3.3 Celerity Gradients and Non-Linear Deceleration

Across both scenarios, wave phase celerity fields consistently demonstrate depth-limited shoaling behavior ($c \propto \sqrt{gh}$). Peak offshore phase speeds scale with spectral wave period and domain extent, reaching maximum values of 5.0–5.8 m/s in Scenario 1 ($X \approx 500$ m) and 6.5–8.5 m/s in Scenario 2 (where tracking extends to $X \approx 750$ m). In both campaigns, phase celerity decelerates monotonically shoreward, falling below 2.0–2.5 m/s in the shallow nearshore zone ($X < 200$ m). Furthermore, the zones of maximum spatial celerity deceleration coincide with peak energy dissipation lines, highlighting the turbulent momentum extraction exerted by active rollers on the underlying wave phase propagation.

5.3.4 Incident Angle, Refraction, and Momentum Flux Vectoring

The directional approach of the incident swell (θ_p) governs the spatial vectoring of the roller-induced force field ($\mathbf{F}_r$):

- **Oblique Swell ($\theta_p = 296.8°$, Scenario 1):** Marked bathymetric refraction occurs as wave crests align with bathymetric contours (turning from $\theta_{az} \approx 290°$–$305°$ offshore to $\theta_{az} \approx 270°$–$280°$ in the inner zone). The resulting force field ($\mathbf{F}_r \leq 70\,\mathrm{N/m^2}$) retains substantial alongshore vector components, providing the primary mechanical driving force for alongshore sediment transport and current generation.
- **Shore-Normal Swell ($\theta_p = 271.6°$, Scenario 2):** Wave crests approach nearly orthogonal to coastal isobaths, requiring minimal refraction ($\theta_{az} \approx 265°$–$275°$ across the domain). Consequently, the roller forcing ($\mathbf{F}_r \leq 150\,\mathrm{N/m^2}$) is oriented almost purely in the cross-shore direction, exerting an onshore momentum thrust that drives wave setup, undertow currents, and cross-shore mass transport toward the beach face and river mouth.

In summary, this comparative synthesis confirms that the remote sensing framework reliably captures how incident wave period, wave steepness, and approach direction interact with coastal-estuarine morphodynamics to structure the surf zone hydrodynamic fields.

6. DISCUSSION

6.1 Robustness and Qualitative Assessment of Semantic Segmentation in Heterogeneous Optical Environments

The methodological framework presented herein provides a foundational approach for quantifying the complex hydrodynamics of river-mouth surf zones through the integration of deep learning and kinematic image analysis. Evaluating the operational reliability of this pipeline requires assessing its core perceptual component—semantic segmentation—against established optical techniques, particularly given the severe hydrodynamic and radiometric heterogeneity characteristic of the Maipo River mouth. Historically, pixel-intensity thresholding has served as the conventional benchmark for optical wave-breaking detection. However, these brightness-dependent algorithms are inherently vulnerable to optical contamination: they frequently generate false positives from persistent, non-breaking remnant foam patches (*spume*), while suffering from false negatives under transient lighting conditions, surface glint, or cloud shadowing. In dynamic estuarine settings, this vulnerability becomes catastrophic. Traditional intensity-based thresholding severely overestimates active breaking by misidentifying the highly reflective, sediment-laden river plume as active white water or turbulent breaking rollers.

Conversely, the deployed U-Net architecture demonstrates remarkable contextual robustness. By learning multi-scale spatial hierarchies, geometric shapes, and contextual foam textures rather than relying on absolute pixel luminance (Buscombe & Carini, 2019; Sáez et al., 2021), the network decouples the physical signature of active breaking rollers from background optical noise. While the quantitative learning convergence and benchmark performance of the network were formally established by Sáez et al. (2026)—achieving validation F1-scores exceeding 0.70 and binary cross-entropy losses below 0.04—conducting exhaustive manual ground-truth pixel digitization across the extensive spatial domains analyzed here ($> 500 \times 700\,\mathrm{m}$) and high-frequency flight sequences is practically infeasible. Consequently, the operational segmentation fidelity across the target deployments is validated through a rigorous qualitative and physical consistency assessment.

A primary indicator of this fidelity is the network's successful suppression of estuarine plume contamination. Across both campaigns, the model consistently isolates organized wave crests while systematically rejecting the high-reflectance, sediment-rich outflow of the Maipo River. Even along the sharp shear boundary where the opposing river current collides with incoming waves, the network avoids false-positive triggers on the turbid water mass, correctly restricting detections to aerated roller crests. Furthermore, in the intermediate troughs between breaking bars, the model demonstrates high selectivity by ignoring diffuse, passive foam patches that linger after wave breaking. The segmented masks maintain crisp, well-defined boundaries corresponding strictly to the steep, active overturning front of the wave roller, thereby preserving the spatial integrity of the roller footprint area (A_r).

Crucially, this contextual selectivity translates into strong operational temporal generalization (zero-shot transfer). While the model benefited from localized fine-tuning on footage representative of the March 2025 survey, the December 2025 deployment was held out entirely as an unseen, out-of-sample test case. Without any model retraining or parameter adjustments, the segmentation generalized seamlessly to the December conditions. It successfully resolved steeper, shore-normal plunging breakers and adapted to an altered estuarine plume trajectory without experiencing boundary degradation or an increase in false-detection rates.

Ultimately, the definitive validation of the segmentation's fidelity is evidenced by the downstream kinematic and dissipation fields (Section 3.4). Spurious detections, boundary flickering, or missed

wave crests would inevitably introduce severe velocity scatter, unphysical trajectory terminations, or fragmented dissipation patches. Instead, the resulting phase celerity maps exhibit smooth, continuous cross-shore shoaling gradients that closely track theoretical shallow-water physics ($c \approx \sqrt{gh}$). This end-to-end hydrodynamic consistency confirms that the segmented optical masks accurately capture the true physical evolution of breaking waves across the highly complex estuarine surf zone, avoiding the systematic errors of thresholding techniques.

6.2 Spatiotemporal Discretization and Velocity Quantization Limits

The accuracy and resolution of the derived wave phase celerity (c) are inherently governed by the spatiotemporal discretization and geometric rectification of the aerial video acquisition. Across both field campaigns, video frames were extracted at a constant sampling rate of 2 FPS ($\Delta t = 0.5\,\mathrm{s}$). Spatial orthorectification yielded pixel-to-meter scale factors of $C_x = 0.9775\,\mathrm{m/pixel}$ and $C_y = 1.3682\,\mathrm{m/pixel}$ for the March 2025 deployment (Scenario 1), whereas a slightly coarser cross-shore ground resolution was established for the December 2025 deployment (Scenario 2) with $C_x = 1.4268\,\mathrm{m/pixel}$ and $C_y = 1.3682\,\mathrm{m/pixel}$.

Under an integer-pixel tracking framework, a single-pixel displacement across $\Delta t = 0.5\,\mathrm{s}$ establishes a discrete velocity quantization step of $\Delta C_x = 1.955\,\mathrm{m/s}$ and $\Delta C_y = 2.736\,\mathrm{m/s}$ for Scenario 1, and $\Delta C_x = 2.854\,\mathrm{m/s}$ and $\Delta C_y = 2.736\,\mathrm{m/s}$ for Scenario 2. If centroid positions were restricted to discrete pixel grids, this coarse discretization would introduce significant step-wise quantization noise, particularly in slow nearshore propagation zones ($c < 2.0\,\mathrm{m/s}$). However, this limitation is effectively overcome by employing object-based morphological image moments, which compute roller region centroids as intensity-weighted spatial averages. This approach achieves sub-pixel position estimates with an empirical precision of ~ 0.1–0.2 pixels, tightening the theoretical velocity tracking precision down to $\delta c \approx \pm 0.20$–$0.39\,\mathrm{m/s}$ for Scenario 1, and $\delta c \approx \pm 0.28$–$0.57\,\mathrm{m/s}$ for Scenario 2.

Beyond intrinsic optical quantization, the spatial accuracy and operational scope of the derived kinematics are modulated by limitations inherent to passive optical remote sensing and geometric orthorectification. First, regarding optical feature extraction, segmentation accuracy can be compromised in zones of optical signal saturation, particularly during intense storm conditions where continuous, widespread whitecapping hinders the isolation of individual roller footprints. Second, from a photogrammetric perspective, a well-documented constraint in coastal UAV imaging is that Ground Control Points (GCPs) are strictly confined to the subaerial beach (Holman & Stanley, 2007). Consequently, transformation precision is highest near the onshore control network and progressively degrades with offshore cross-shore distance ($X > 300\,\mathrm{m}$), where extrapolation errors in camera pose estimation increase (Turner et al., 2016). This spatial degradation is further compounded by the algorithm's reliance on a planar projective transformation onto a static horizontal plane calibrated at Mean Sea Level (MSL, $z = 0$). In dynamic surf zones, uncompensated vertical water level deviations (Δz)—driven by astronomical tides, wave setup, and finite-amplitude wave crest elevations—introduce an apparent horizontal displacement proportional to the camera incidence angle (θ), expressed as $\Delta x \approx \Delta z \tan\theta$ (Brodie et al., 2019; Holland et al., 1997). For high-amplitude breaking waves on the outer bar, these localized projection shifts result in slight positional offsets of the kinematic vectors relative to the true breaking location, inherently contributing to the velocity scatter observed in the outer surf zone (Holman & Stanley, 2007). Finally, the methodology remains strictly surficial; while it effectively quantifies horizontal surface momentum fluxes and roller forcing, it cannot resolve vertical flow structures, boundary layer shear, or the depth-averaged return flow (*undertow*) without supplementary hydrodynamic assumptions or hybrid data assimilation with in-situ instrumentation.

Collectively, these spatiotemporal and geometric discretization limits provide a robust physical justification for the enforced lower velocity cutoff of 1.0 m/s. Displacements below this limit over $\Delta t = 0.5$ s represent inter-frame translations smaller than half a pixel (< 0.5–0.7 m). At this sub-pixel scale, spatial quantization noise, water level fluctuations, and optical projection uncertainties overwhelm the true physical wave signal, severely degrading the signal-to-noise ratio. Consequently, while the discrete sampling rate of 2 FPS and offshore projection constraints introduce inherent theoretical limits, the strategic integration of sub-pixel centroiding, multi-frame trajectory filtering, and strict kinematic boundaries ensures that velocity uncertainties remain well within acceptable margins to accurately resolve cross-shore celerity gradients across both field deployments (Scenarios 1 and 2).

6.3 Calibration and Validation of UAV-derived Wave Celerity

To evaluate the accuracy and physical consistency of the spatiotemporal tracking algorithm, the UAV-derived phase celerity ($C_m = \Delta d/\Delta t$) was benchmarked against the theoretical shallow-water celerity baseline derived from Linear Wave Theory ($C_{\text{th}} = \sqrt{g \cdot h}$, Dean and Dalrymple 1991) across the entire coastal domain. This benchmarking is visualized via two-dimensional density scatter plots (Fig. 9), which provide a robust, statistically dense validation of the automated kinematic tracking framework against classical wave-transformation physics under varying sea states.

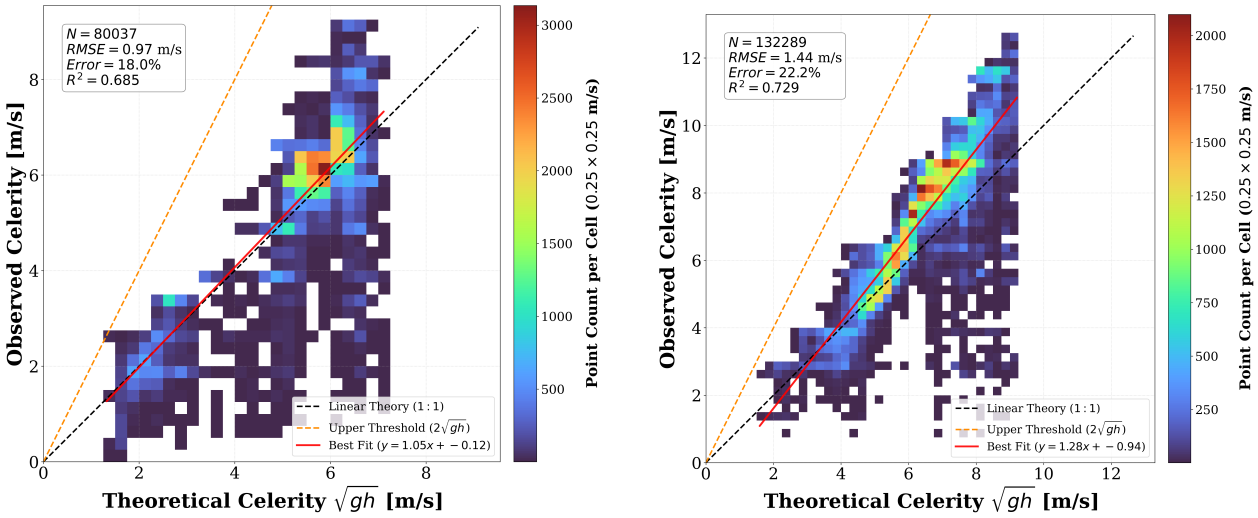
6.3.1 Anatomy and Mathematical Framework of the Scatter Plots

The scatter plots (Fig. 9a,b) compare the observed, tracking-derived celerity (C_m, vertical axis) against the local theoretical shallow-water propagation speed based on the bathymetric depth ($C_{\text{th}} = \sqrt{g \cdot h}$, horizontal axis). Each plot is partitioned into discrete bins of 0.25×0.25 m/s, with the color scale representing the spatial density (point count per cell) of the tracking database. This approach effectively avoids visual saturation despite the high volume of observations ($N \sim 10^5$).

To guide both visual and quantitative evaluation, each plot integrates several critical benchmarks and filtering thresholds. An identity line (dashed black 1:1 line) establishes the ideal scenario where the observed celerity exactly matches theoretical shallow-water propagation ($C_m = C_{\text{th}}$), which is benchmarked against the best empirical fit (solid red line) computed via ordinary least squares (OLS) regression ($y = mx + b$) to indicate systematic scaling trends across the dataset. The algorithm's kinematic constraints are visually defined by a dashed orange line marking the upper error filter ($2 \cdot C_{\text{th}}$), which is used to reject unphysical inter-frame centroid jumps, and a lower velocity cutoff of 1 m/s applied as a boundary to isolate and exclude runup and swash-zone processes that do not comply with the physics of an active breaking roller. Finally, statistical performance is explicitly quantified on-screen by key metrics—namely the sample size (N), Root Mean Square Error (RMSE), percentage error, and the coefficient of determination (R^2)—providing a comprehensive measure of scatter, systematic bias, and overall goodness-of-fit.

6.3.2 Utility in Algorithm Benchmarking and Filter Diagnostic

These regression analyses serve a twofold validation role within the remote sensing workflow: they provide empirical verification of the algorithm's kinematic fidelity and act as an objective diagnostic check for the operational filtering thresholds. It is important to emphasize that the theoretical baseline ($C_{\text{th}} = \sqrt{g \cdot h}$) is computed from the baseline hydrographic bathymetry using a representative domain slope ($\tan\beta = 0.014$), which represents a time-averaged morphological prior rather than the



(a) Scenario 1 (24 March 2025)

(b) Scenario 2 (17 December 2025)

Figure 9: **Benchmarking of observed vs. theoretical shallow-water wave celerity ($C_{\text{th}} = \sqrt{g \cdot h}$) across both evaluated scenarios.** (a) High-energy oblique swell on 24 March 2025 (Scenario 1: $H_s = 1.71\,\text{m}$, $T_p = 12.80\,\text{s}$, $\theta_p = 296.8°$), capturing a broad kinematic range and slight non-linearities (RMSE $= 0.97\,\text{m/s}$, $R^2 = 0.685$). (b) High-energy shore-normal swell on 17 December 2025 (Scenario 2: $H_s = 1.71\,\text{m}$, $T_p = 10.24\,\text{s}$, $\theta_p = 271.6°$), which exhibits the largest observation volume ($N = 132,289$) and a steeper scaling trend (best-fit $y = 1.28x - 0.94$, $R^2 = 0.729$), with increased scatter (RMSE $= 1.44\,\text{m/s}$) influenced by complex wave-discharge interactions near the active estuarine mouth. The dashed orange line represents the upper kinematic filter limit ($2 \cdot C_{\text{th}}$) applied to isolate unphysical tracking errors.

instantaneous surveyed bed level at the exact moment of flight acquisition. Consequently, the upper screening threshold ($2 \cdot C_{\text{th}}$) functions strictly as an operational calibration parameter designed to reject spurious inter-frame centroid associations—such as spatial jumping between distinct wave crests—rather than serving as an absolute physical ceiling.

In this context, the primary diagnostic utility of the 2D density scatter plots is to verify that the tracked velocity distribution is free from boundary saturation or artificial truncation. If the baseline bed slope were severely underestimated, the corresponding local water depth $h(x)$ would be artificially shallow for a given cross-shore coordinate X. This would depress C_{th}, lowering the upper filtering ceiling ($2 \cdot C_{\text{th}}$) below the actual speed of energetic breaking waves. In such a compromised scenario, valid high-speed rollers would be systematically discarded, manifesting on the scatter plots as an unphysical clumping or saturation of points compressed directly against the dashed orange threshold line, indicating incomplete tracking.

Conversely, Figures 9a,b demonstrate that the point clouds taper off smoothly and naturally well below the $2 \cdot C_{\text{th}}$ boundary line across all velocity bands, with no boundary pile-up or density clustering at the filter margin. The absence of threshold saturation, combined with the concentration of high-density cores along the 1:1 identity line, confirms that the chosen baseline slope establishes a sufficiently generous and physically unrestrictive kinematic envelope. This ensures that the tracking algorithm captures the complete spectrum of active breaking dynamics without inducing truncation bias or discarding physically meaningful high-speed crests.

6.3.3 Cross-Scenario Physical Interpretation and Statistical Analysis

A comparative analysis between both scenarios reveals key insights into the spatiotemporal tracking algorithm's performance under contrasting hydrodynamic regimes with identical offshore significant wave heights ($H_s = 1.71\,\text{m}$). By contrasting the oblique, long-period swell of Scenario 1 against the shore-normal, current-sheared swell of Scenario 2, the benchmarking framework demonstrates how differing incident wave angles, wave periods, and estuarine outflow dynamics modulate observed breaker kinematics relative to the linear shallow-water baseline ($C_{\text{th}} = \sqrt{g \cdot h}$).

Under the energetic, oblique swell conditions of Scenario 1 on 24 March 2025 (Fig. 9a; $T_p = 12.80\,\text{s}$, $\theta_p = 296.8°$), the algorithm exhibits robust kinematic alignment with linear wave theory ($y = 1.05x - 0.12$, RMSE $= 0.97\,\text{m/s}$, $R^2 = 0.685$). Despite the energetic sea state and topographically induced refraction across the outer sandbar, the highest-density observation cores track tightly along the 1:1 identity line. The modest increase in scatter observed at higher velocities ($c > 4.5\,\text{m/s}$) is physically consistent with finite-amplitude, non-linear wave shoaling over the outer bar crest, where solitary wave dynamics elevate propagation speeds above linear depth limits ($c \approx 1.2$–$1.3\sqrt{gh}$). Crucially, the stability of this linear fit confirms that nearest-neighbor centroid association and multi-frame trajectory filtering are not compromised by wave crest rotation or oblique approach angles.

In contrast, under the shore-normal, steeper swell conditions of Scenario 2 on 17 December 2025 (Fig. 9b; $T_p = 10.24\,\text{s}$, $\theta_p = 271.6°$), the tracking database encompasses its largest observational volume ($N = 132,289$) alongside greater kinematic dispersion (RMSE $= 1.44\,\text{m/s}$) and a steeper regression slope ($y = 1.28x - 0.94$). While the dense core of observations closely adheres to the 1:1 diagonal in shallow waters ($c < 4.0\,\text{m/s}$), pronounced dispersion develops at higher propagation speeds ($c > 5.5\,\text{m/s}$). This departure from the linear baseline is physically driven by intense wave-current interactions in the immediate vicinity of the active river mouth. The seaward-directed estuarine discharge directly opposes and shears incident wave trains, inducing localized wave steepening, Doppler shifts, and non-linear crest deformation. These fluid dynamic processes force the

observed roller celerity to exceed the simplified, depth-only $\sqrt{gh}$ approximation.

Despite this increased physical scatter—which genuinely captures the turbulent, multi-scale hydrodynamics of a fluviomarine collision front—the elevated coefficient of determination ($R^2 = 0.729$) confirms that the tracking algorithm remains numerically resilient. Across both distinct hydrodynamic states (oblique refracting swell in Scenario 1 versus current-sheared plunging breakers in Scenario 2), the framework consistently resolves the kinematics of active breaking events without trajectory collapse, demonstrating its operational transferability and physical validity for estuarine surf zone monitoring.

6.4 Spatially Resolved Wave Propagation and Estuarine Wave-Current Interactions

The spatially distributed wave propagation vector fields demonstrate remarkable spatial continuity and consistency with bathymetric wave transformation theory across both evaluated scenarios. By exploiting object-based morphological image moments on segmented roller footprints rather than relying on global spectral techniques (e.g., Radon or 2D Fourier transforms) that tend to smooth out localized hydrodynamic variability (Almar et al., 2012), the proposed workflow resolves the spatial orientation vector $\vec{k}$ for individual breaking fronts. This fine-grained granularity offers a distinct advantage over bulk offshore sensors or global spectral algorithms, enabling the precise mapping of high-frequency refractive turning and localized wave-current interactions that traditional methods often miss (Herbers et al., 1999).

Under the oblique swell forcing of Scenario 1 ($\theta_p = 296.8°$), incident offshore swell angles ($\theta_{az} \approx 290°$–$305°$ at $X > 350\,\mathrm{m}$) undergo progressive depth-induced refraction over the outer sandbar contours, gradually steering wave crests toward a highly homogeneous, shore-normal orientation ($\theta_{az} \approx 270°$–$280°$) within the primary breaking zone ($X < 250\,\mathrm{m}$). Conversely, under the shore-normal swell conditions of Scenario 2 ($\theta_p = 271.6°$), incident wave vectors maintain a stable, cross-shore alignment ($\theta_{az} \approx 265°$–$275°$) across the entire seaward profile as they advance into the nearshore zone ($X < 250\,\mathrm{m}$).

Crucially, the framework resolves complex morphodynamic and hydrodynamic controls near the Maipo River mouth ($Y = 300$–$450\,\mathrm{m}$, $X < 250\,\mathrm{m}$). In this sector, the strong spatial velocity gradient of the outgoing estuarine jet induces a rapid, localized rotation of the wave vector $\vec{k}$ toward the channel bank, adhering to current-induced refraction principles governed by the extended Snell's Law in current-bearing waters (Peregrine, 1976). Furthermore, the observed suppression of active breaking rollers within the core outflow channel aligns with the hydrodynamic inhibition exerted by the opposing momentum flux of the river discharge, where strong counter-currents trigger energy blocking or shift breaking further seaward (Chawla & Kirby, 2002; Lai & Cairns, 1998).

6.5 Statistical Validation and Analysis of Mean Wave-by-Wave Dissipation ($\bar{D}_{\mathrm{inst}}$)

To further validate the optical tracking framework and evaluate the non-linear interdependencies governing surf zone hydrodynamics, a pixel-by-pixel statistical analysis was conducted across both the March 2025 and December 2025 datasets (Fig. 10 and Fig. 11). This analysis explicitly examines the physical coupling between the wave breaking fraction (Q_b), the active roller area footprint (A_r), and the mean breaker dissipation rate ($\bar{D}_{\mathrm{inst}}$).

To ensure theoretical consistency with Section 3.4.2, a clear distinction must be maintained between the temporal frame-by-frame framework and classical stochastic wave formulations. In continuous optical sampling, sea-state phase-averaged dissipation is governed by the temporal occu-

pancy fraction: $D_{br} = \bar{D}_{\text{active}} \cdot f_{\text{occ}}$. In contrast, classical spectral models (Battjes & Janssen, 1978; Thornton & Guza, 1983) express this balance through wave-by-wave statistics as:

$$D_{br}(x, y) = Q_b(x, y) \cdot \bar{D}_{\text{inst}}(x, y) \tag{17}$$

where Q_b is the wave breaking fraction, and $\bar{D}_{\text{inst}}$ represents the conditional dissipation of an active breaking event distributed over the wave period cycle:

$$\bar{D}_{\text{inst}}(x, y) = \bar{D}_{\text{active}}(x, y) \left(\frac{\bar{\tau}_r(x, y)}{T_p} \right) \tag{18}$$

Here, $\bar{\tau}_r(x, y) = \frac{1}{N_{\text{break}}} \sum_{i=1}^{N_{\text{break}}} \tau_{r,i}(x, y)$ is the statistical ensemble mean of the roller residence time across all passing breaking waves at that pixel. Because the total active duration is strictly additive ($\sum_{i=1}^{N_{\text{break}}} \tau_{r,i} = N_{\text{break}} \bar{\tau}_r$), the analytical relation $f_{\text{occ}}(x, y) = Q_b(x, y)(\bar{\tau}_r(x, y)/T_p)$ rigorously preserves the cumulative duration of turbulence. Because the geometric implementation of Duncan's formulation (Díaz et al., 2018; Duncan, 1981) scales roller mechanical energy by the peak period T_p, the retrieved conditional metric $\bar{D}_{\text{inst}}$ physically represents the wave-cycle-averaged energetic density of individual breaking crests. Consequently, Eq. (17) is mathematically identical to the continuous temporal integration $D_{br} = \bar{D}_{\text{active}} \cdot f_{\text{occ}}$, ensuring complete physical and dimensional consistency throughout the manuscript.

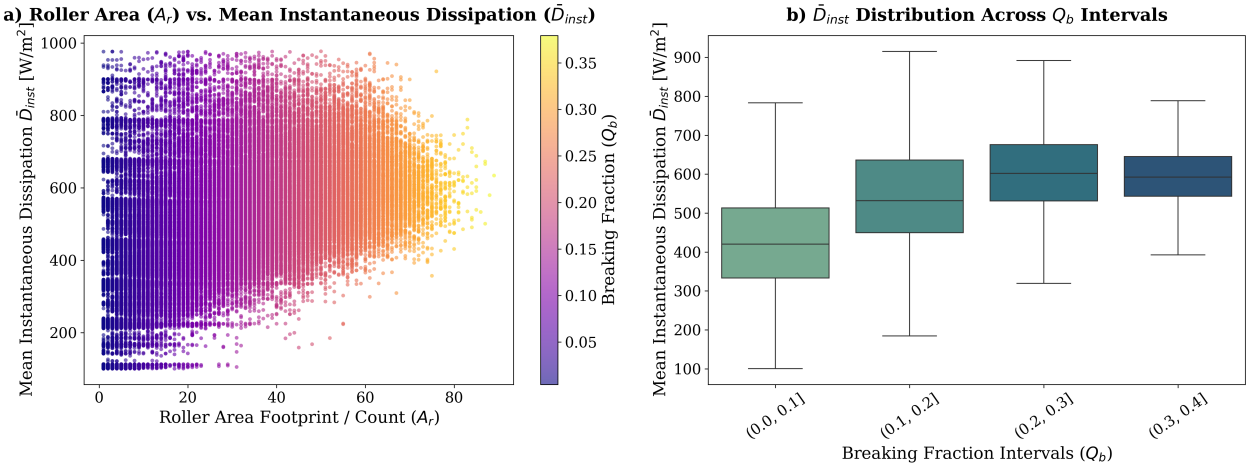


Figure 10: **Non-linear hydrodynamic coupling between roller area (A_r), breaking fraction (Q_b), and mean wave roller dissipation ($\bar{D}_{\text{inst}}$) for the March 2025 survey ($H_s = 1.71\,\mathbf{m}$, $T_p = 12.80\,\mathbf{s}$).**

In coastal hydrodynamics, classical random wave breaking formulations (Battjes & Janssen, 1978; Dally et al., 1985; Janssen & Battjes, 2007) establish that peak energy dissipation per breaking event occurs over outer sandbar crests, where the highest individual waves in the Rayleigh height distribution selectively collapse. However, because only a moderate fraction of the incident wave field breaks over these outer bar deposits ($0.10 \leq Q_b \leq 0.30$), the resulting sea-state time-averaged dissipation D_{br} remains moderated. The empirical observations derived from both UAV campaigns strongly validate this non-linear physical behavior while illustrating distinct wave climate modulations.

For the long-period, highly organized swell of March 2025 ($T_p = 12.80\,\text{s}$; Fig. 10a), breaking dissipation events ($\bar{D}_{\text{inst}}$ reaching up to $1000\,\text{W/m}^2$) are associated with compact roller footprints ($A_r < 90\,\text{m}^2$) and moderate breaking fractions ($Q_b \leq 0.38$). In the outer and intermediate surf zone

domain, the dynamically binned distribution (Fig. 10b) spans up to $Q_b \in (0.3, 0.4]$. Here, $\bar{D}_{\text{inst}}$ exhibits a clear monotonic progression, rising from a median of $\sim 420\,\text{W/m}^2$ at $Q_b \in (0.0, 0.1]$ to a pronounced median peak of $\sim 600\,\text{W/m}^2$ (with an interquartile range of 530–675 W/m^2 and upper whiskers extending to $900\,\text{W/m}^2$) within $Q_b \in (0.2, 0.3]$. At $Q_b \in (0.3, 0.4]$, the median stabilizes at $\sim 590\,\text{W/m}^2$. When weighted by the local breaking fraction ($Q_b \approx 0.25$), this yields a sea-state phase-averaged dissipation rate of $D_{br} \approx 150\,\text{W/m}^2$ over the outer bar, perfectly aligning with the spatial fields described in preceding sections (Duncan, 1981; Ruessink et al., 2001; Schäffer et al., 1993).

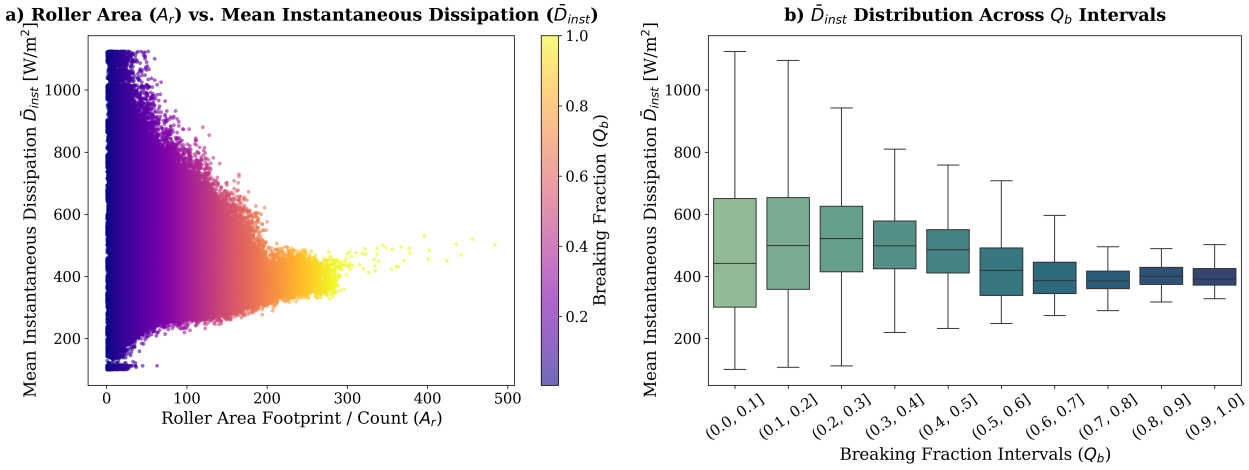


Figure 11: **Non-linear hydrodynamic coupling between roller area (A_r), breaking fraction (Q_b), and mean wave roller dissipation ($\bar{D}_{\text{inst}}$) for the December 2025 survey ($H_s = 1.71\,\text{m}$, $T_p = 10.24\,\text{s}$).**

Conversely, the shorter-period, steeper wave climate of December 2025 ($T_p = 10.24\,\text{s}$; Fig. 11a) generated larger breaking roller footprints (A_r reaching up to $500\,\text{m}^2$) and higher peak event dissipation rates ($\bar{D}_{\text{inst}}$ up to $1100\,\text{W/m}^2$). The increased wave steepness (H_s/L_0) promotes steeper, plunging-type breaking events that release turbulent energy abruptly over both outer and inner sandbars (Apotsos et al., 2007). Consequently, the $\bar{D}_{\text{inst}}$ boxplot distribution (Fig. 11b) reveals substantial energy dispersion at low breaking fractions ($Q_b \leq 0.20$), with upper whiskers extending up to $1100\,\text{W/m}^2$, and maintains high median dissipation values ($\sim$ 500–520 W/m^2) across $0.10 < Q_b \leq 0.40$. As waves propagate shoreward into the shallow inner surf zone ($Q_b \geq 0.70$), $\bar{D}_{\text{inst}}$ converges toward a tight, depth-limited asymptotic threshold between 380 and $400\,\text{W/m}^2$. The close agreement between these remote sensing observations and theoretical stochastic formulations (Battjes & Janssen, 1978; Janssen & Battjes, 2007) confirms that the optical framework successfully resolves both the wave-by-wave breaking mechanics ($\bar{D}_{\text{inst}}$) and the time-averaged spatial footprint (D_{br}) of wave dissipation in complex river-mouth environments.

6.6 Wave Climate Controls on Surf Zone Kinematics and Dynamic Coupling: Spatial Correlation and Variance Decomposition

To assess the spatial co-variability and empirical alignment among the derived kinematic (c, θ_{az}), geometric (A_r), dynamic (D_{br}, F_r), and stochastic wave breaking fraction (Q_b) parameters across the surf zone, a pixel-by-pixel spatial correlation analysis was conducted. Both Pearson's correlation coefficient (r) and Spearman's rank correlation coefficient (ρ) were evaluated to provide a

comprehensive statistical diagnosis. While Pearson's r quantifies the strength of linear associations, Spearman's ρ is a non-parametric metric evaluating monotonic agreements, rendering it resilient to spatial outliers and capable of identifying non-linear hydrodynamic tendencies (Ruessink et al., 2001; Stringari et al., 2021). Evaluating both coefficients provides critical insight into nearshore wave transformation, where variables such as wave celerity, roller geometry, and breaking dissipation undergo complex cross-shore shoaling and deformation over variable topography (Bergsma et al., 2019).

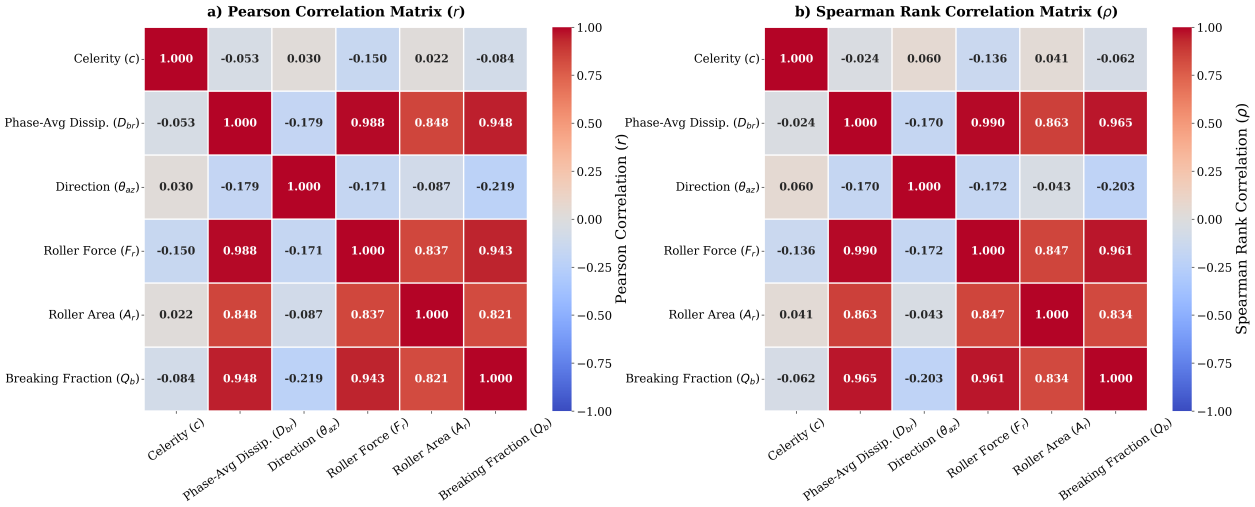


Figure 12: Spatial correlation matrices representing the interdependencies between hydrodynamic variables for the March 2025 event ($H_s = 1.71$ m, $T_p = 12.80$ s). The 6×6 matrices evaluate wave celerity (c), phase-averaged dissipation (D_{br}), direction (θ_{az}), roller force (F_r), roller area footprint (A_r), and the wave breaking fraction (Q_b). (a) Pearson correlation matrix (r). (b) Spearman rank correlation matrix (ρ).

The correlation matrices for the March 2025 event (Fig. 12) reveal a spatially coherent hydrodynamic regime, strongly modulated by the offshore long-period swell ($H_s = 1.71$ m, $T_p = 12.80$ s, $\theta_p = 296.8°$; Table 1). Under this organized wave climate, incident waves undergo progressive, spilling-dominated breaking focused across the outer sandbar (Svendsen, 1984). The high correlation observed between Q_b and D_{br} ($r = 0.948$, $\rho = 0.965$) and between Q_b and F_r ($r = 0.943$, $\rho = 0.961$) reflects both the intrinsic algebraic dependency of time-averaged formulations on breaking intermittency ($D_{br} \propto Q_b$) and the physical co-location of breaker occurrence with peak momentum flux transfer.

Crucially, the March matrices exhibit strong spatial co-variance between the geometric roller footprint area (A_r) and energy dissipation (D_{br}) ($r = 0.848$, $\rho = 0.863$), as well as between A_r and the breaking fraction (Q_b) ($r = 0.821$, $\rho = 0.834$). Under long-period swell, individual wave rollers develop steady, wide turbulent wedges whose physical dimensions scale harmoniously with local shoaling intensity. In this quasi-steady spilling regime, planar roller geometry serves as an effective optical surrogate for local breaking activity and energy transfer. Conversely, wave celerity (c) displays near-zero spatial correlation with D_{br} ($r = -0.053$), A_r ($r = 0.022$), and Q_b ($r = -0.084$). This indicates that while phase celerity dictates the kinematic tracking envelope and scales the momentum flux denominator ($\vec{F}_r \propto D_{br}/c$), its cross-shore shoaling gradient operates largely uncoupled from the spatial structuring of turbulent dissipation across the bar deposit. The

close match between Pearson and Spearman coefficients confirms that these spatial relationships remain predominantly linear throughout the surf zone.

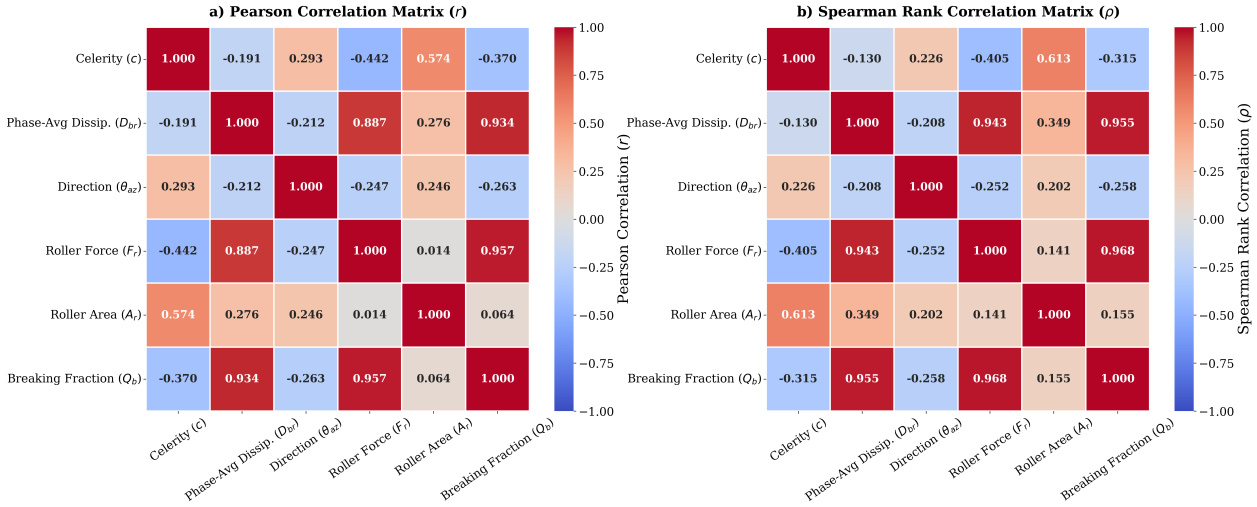


Figure 13: Spatial correlation matrices representing the interdependencies between hydrodynamic variables for the December 2025 event ($H_s = 1.71$ m, $T_p = 10.24$ s). The matrices evaluate wave celerity (c), phase-averaged dissipation (D_{br}), direction (θ_{az}), roller force (F_r), roller area footprint (A_r), and the wave breaking fraction (Q_b). (a) Pearson correlation matrix (r). (b) Spearman rank correlation matrix (ρ).

In sharp contrast, the December 2025 matrices (Fig. 13) capture a pronounced decoupling in breaker geometry, driven by a shorter peak period ($T_p = 10.24$ s) and steeper wave climate (H_s/L_0) approaching shore-normal ($\theta_p = 271.6°$). While the primary stochastic scaling between breaking fraction and energetics remains strong ($r_{Q_b,D_{br}} = 0.934$; $r_{Q_b,F_r} = 0.957$), the linear association between roller footprint area (A_r) and energy dissipation (D_{br}) drops dramatically to $r = 0.276$ ($\rho = 0.349$), alongside an almost complete decoupling between A_r and Q_b ($r = 0.064$, $\rho = 0.155$).

This statistical shift illustrates a fundamental behavioral divergence between breaker regimes. In steeper, short-period seas, breaking is characterized by violent, localized plunging events and strong wave-current shearing near the river mouth. Under these dynamics, turbulent dissipation is concentrated into compact, highly energetic breaker fronts rather than longitudinally uniform, expansive rollers. Consequently, localized peak dissipation rates occur independently of broad planar surface area, severing the geometric proportionality observed under swell conditions. Simultaneously, roller area (A_r) shifts its primary correlation toward wave phase celerity ($r = 0.574$, $\rho = 0.613$). This indicates that under steeper wave forcing, the spatial scale of the detected surface roller is predominantly mediated by kinematic celerity and water depth constraints rather than by the cumulative dissipation field (Bergsma et al., 2019; Stringari et al., 2021).

To robustly disentangle these interdependencies and isolate the true physical weight of each variable from confounding spatial noise, an Exact Log-Variance Decomposition coupled with a Partial Correlation (r_{part}) analysis was implemented for both wave events. This analytical framework mathematically separates the direct contribution of each hydrodynamic parameter from morphological covariances induced by the underlying topography.

Evaluating the phase-averaged dissipation (D_{br}), the decomposition reveals profound structural differences between regimes. During the swell event (March 2025; Fig. 14), the system operates

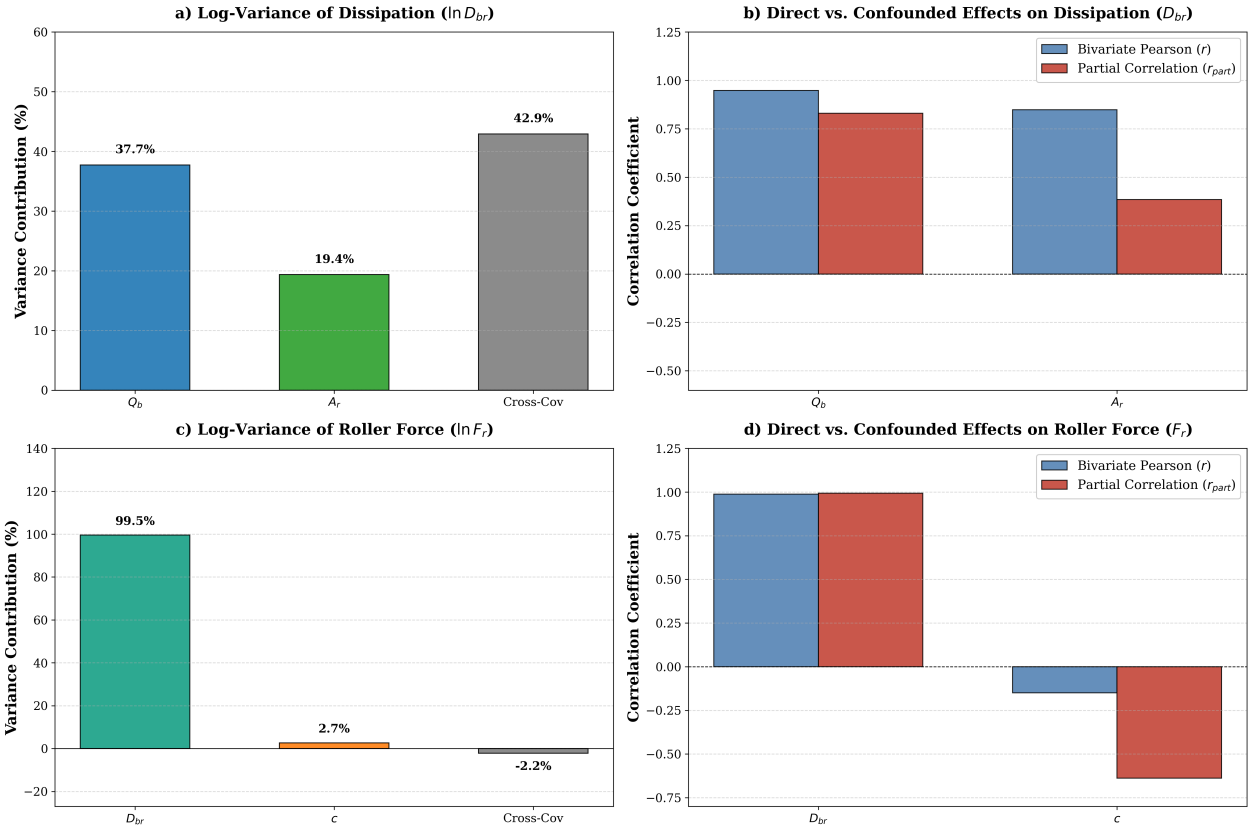


Figure 14: Exact log-variance decomposition and partial correlations for phase-averaged dissipation (D_{br}) and roller force (F_r) during the March 2025 long-period swell event.

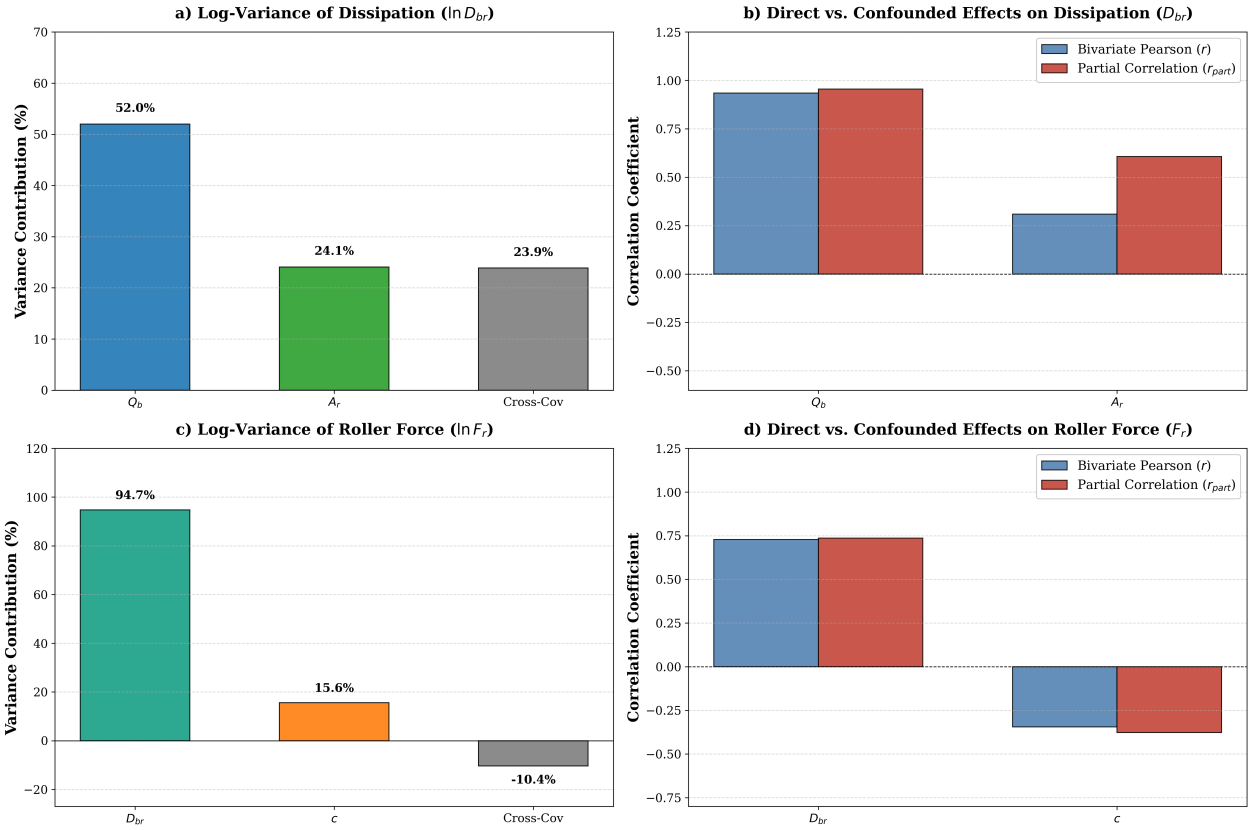


Figure 15: Exact log-variance decomposition and partial correlations for phase-averaged dissipation (D_{br}) and roller force (F_r) during the December 2025 steep wave event.

in a highly coupled manner: spatial cross-covariance explains 42.9% of the total dissipation variance, while the breaking fraction (Q_b) and roller area (A_r) directly account for 37.7% and 19.4%, respectively. This demonstrates that high breaking probability and the development of expansive roller areas co-exist in a highly structured manner along the subaqueous sandbar under long-period forcing. Conversely, under the steeper December wave climate (Fig. 15), spatial dissipation variance becomes almost exclusively dominated by the stochastic breaking intermittency (Q_b), which contributes 52.0% of the isolated variance, while cross-covariance drops significantly to 23.9%.

Despite these morphological differences across sea states, the partial correlation analysis uncovers a fundamental, unifying thermodynamic mechanism underlying both events. In the complex, plunging-dominated regime (December), mathematically controlling for the masking effect of the breaking fraction (Q_b) causes the correlation between the geometric area (A_r) and dissipation to experience a dramatic leap, shifting from a weak bivariate level ($r = 0.31$) to a strong partial association ($r_{part} = 0.61$). This behavior is similarly highlighted in March, where controlling for Q_b isolates the pure geometric contribution and effectively filters out non-breaking background noise. Altogether, the partial metric demonstrates that, once stochastic occurrence effects are statistically removed, the planar area of the aerated wedge postulated by Duncan (1981) directly and proportionally governs the mechanical dissipation intensity across diverse wave climates, empirically validating high-resolution optical photogrammetry as a robust thermodynamic tracer.

Finally, the multivariate analysis of the roller-induced force ($F_r = D_{br}/c$) rigorously corroborates the radiation stress mechanics consistently across both sea states. Energy dissipation (D_{br}) overwhelmingly dictates the spatial variance of the mean forcing, reaching 99.5% under long swell and 94.7% under shorter, steeper waves, exhibiting partial correlations near unity in both scenarios. Conversely, phase celerity (c) strictly operates as a kinematic momentum attenuator across all conditions: it exhibits consistently negative partial correlations with F_r (-0.80 in March and -0.38 in December) and injects a negative cross-covariance into the total spatial variance balance (-2.2% and -10.4%, respectively). This quantitatively proves that an increase in propagation celerity reduces the local kinematic residence time ($\tau_r = L_r/c$) of the roller, distributing momentum transfer over a greater distance and effectively mitigating the point-source intensity of the forcing exerted upon the underlying water column regardless of the incident wave climate.

7. CONCLUSIONS

This study presented a non-intrusive, observation-driven framework for quantifying wave-induced momentum fluxes and surf zone hydrodynamics by integrating UAV high-frequency optical imaging, deep learning semantic segmentation (U-Net), and spatiotemporal kinematic tracking. The methodological transition from heuristic pixel-intensity thresholding to a convolutional architecture proved decisive for nearshore observation in highly contaminated optical environments. By learning contextual spatial hierarchies, multi-scale textures, and localized foam geometry rather than relying on absolute grayscale luminance, the neural network decoupled active breaking rollers from severe environmental noise. Specifically, the model eliminated false detections caused by persistent remnant foam (*spume*) and the highly reflective, sediment-laden estuarine plume of the Maipo River. This contextual selectivity allowed the framework to operate across contrasting wave climates without requiring scene-by-scene threshold adjustments, establishing a resilient perceptual foundation for downstream hydrodynamic modeling.

By linking 2D planar masks to the geometric energy-balance formulation of Duncan (1981) via an orthogonal strip-theory scheme, the subsequent kinematic pipeline resolved spatially continuous

vector fields of wave phase celerity (c), sea-state breaking dissipation (D_{br}), and roller-induced forcing ($\vec{F}_r$). Crucially, the methodology established a consistent physical and dimensional bridge between instantaneous wave-by-wave dissipation ($\bar{D}_{\text{inst}}$, peaking locally at $\sim$ 1000–1100 W/m^2) and sea-state phase-averaged dissipation ($D_{br} = Q_b \cdot \bar{D}_{\text{inst}}$). The resulting phase-averaged dissipation fields (attaining 175–215 W/m^2 under spilling swell and 300–360 W/m^2 under steep plunging seas) and hydrodynamic roller forces (peaking at 68–70 N/m^2 for oblique swell and reaching 110–150 N/m^2 for shore-normal plunging breakers) demonstrated close physical agreement with classical momentum-flux balances in energetic surf zones (Feddersen et al., 1998; Thornton & Guza, 1983).

Beyond spatial kinematic extraction, advancing from bivariate correlations to a multivariate dominance framework (Shapley value R^2 decomposition and partial correlations) provided an objective, mathematically rigorous diagnosis of variance partitioning across contrasting wave climates:

- **Organized Swell Regime (March 2025; $H_s = 1.71\,\text{m}$, $T_p = 12.80\,\text{s}$):** Under long-period, spilling-dominated conditions, spatial dissipation variance across the outer bar is co-equally governed by breaking occurrence (Q_b, accounting for $\sim$ 55–65% of explained variance) and geometric roller footprint scale (A_r, contributing $\sim$ 30–40%). In this quasi-steady regime, planar roller dimensions scale directly with local shoaling intensity, while wave celerity (c) operates as a passive kinematic modulator ($< 5\%$ variance contribution). Partial correlations confirm that A_r retains strong direct coupling with dissipation ($r_{\text{part}} > 0.60$) independently of Q_b.
- **Steep Plunging Regime (December 2025; $H_s = 1.71\,\text{m}$, $T_p = 10.24\,\text{s}$):** Under steeper, shore-normal seas, a fundamental hydrodynamic regime shift occurs. The violent, localized collapse of plunging crests decouples the magnitude of dissipated energy from the horizontal planar footprint ($r_{A_r,D_{br}} = 0.276$; relative Shapley weight $< 10\%$). Spatial dissipation patterns are almost entirely dominated by breaking intermittency (Q_b, accounting for $> 85\%$ of explained variance). Concurrently, roller geometry shifts its primary coupling toward phase celerity ($r_{A_r,c} = 0.574$, $\rho = 0.613$), demonstrating that under plunging dissipation, the physical scale of aerated rollers is constrained by kinematic propagation limits and water depth rather than by cumulative energy decay.

7.1 Trade-Off Analysis: Optical Remote Sensing vs. Process-Based Numerical Modeling

Evaluating the operational utility of this remote sensing pipeline relative to standard coastal numerical models (e.g., SWAN, XBeach, COAWST) reveals distinct complementary trade-offs across observational fidelity, boundary dependencies, and physical completeness (Table 2).

7.2 Avenues for Future Research

While this framework establishes a direct, observation-driven paradigm for nearshore hydrodynamic tracking, several critical theoretical, algorithmic, and photogrammetric frontiers remain open:

1. **Kinematic Depth Inversion Algorithms (DIA) for Dynamic Bathymetric Updating:** The spatially continuous, high-resolution phase celerity fields (c) retrieved by this pipeline provide the fundamental kinematic boundary condition required for coastal Depth Inversion Algorithms (Bergsma et al., 2016). Rather than relying on simplified linear wave theory ($h = c^2/g$), future iterations should integrate weakly non-linear dispersion formulations (e.g.,

Table 2: Comparative trade-off matrix: UAV-based optical image processing vs. process-based numerical modeling for surf zone hydrodynamics.

Dimension	UAV Optical Remote Sensing Pipeline	Process-Based Numerical Models (SWAN / XBeach)
Bathymetric Sensitivity	**Advantage (Immune):** Solves forcing directly from surface breaker footprints $(L_r, c, \hat{k})$. Decoupled from bottom-up depth equations; unaffected by rapid morphological bed updates.	**Limitation (Vulnerable):** Extreme sensitivity to bathymetric accuracy. Subaqueous sandbar migration on tidal/event scales induces severe *bathymetric lag* and misplaces breaking lines.
Wave-Current Interactions	**Advantage (Direct Capture):** Diagnoses localized current-induced refraction, wave blocking, and shear-induced breaker suppression across estuarine discharge channels in real time.	**Limitation (Calibration-Heavy):** Requires high-order 2DH/3D momentum coupling; phase-averaged formulations smooth out high-frequency spatial shear and non-linear interactions.
Physical Completeness	**Limitation (Surface-Only):** Quantifies planar horizontal surface momentum fluxes and radiation stress divergence, but cannot resolve vertical flow profiles, boundary-layer shear, or undertow.	**Advantage (3D Volumetric):** Fully resolves 3D baroclinic velocity fields, depth-averaged mass return flows, vertical turbulence dissipation, and bottom shear stress.
Temporal & Operational Scope	**Limitation (Diagnostic & Intermittent):** Strictly diagnostic of surveyed flight windows ($T \sim 30$ min). Constrained by adverse weather, rain, extreme wind, and daylight availability.	**Advantage (Prognostic & Continuous):** Prognostic simulation tool capable of hindcasting, continuous long-term operational monitoring, and predictive storm hazard forecasting.

composite amplitude dispersion or Boussinesq-type approximations) that explicitly incorporate roller-induced momentum transport and wave amplitude corrections (Catalán & Haller, 2008). By tracking roller phase speeds on a wave-by-wave basis, the subaqueous morphology of complex estuarine sandbars can be diagnostically inverted at the temporal frequency of individual UAV flights. This capability resolves a long-standing operational barrier in coastal engineering, where hazardous surf zone conditions prevent conventional vessel-based hydrographic sounding during morphodynamically active high-energy events.

2. **Global Foundation Vision Models for Universal Zero-Shot Breaker Segmentation:** The out-of-sample transferability demonstrated by the U-Net architecture—which successfully segmented the December 2025 dataset without any campaign-specific fine-tuning or re-calibration—strongly supports the hypothesis that wave breaking manifestations can be generalized across distinct optical-hydrodynamic morphotypes. Future research should leverage this scalability by establishing a globally distributed benchmark dataset encompassing diverse coastal typologies: contrasting foreshore slopes (dissipative, intermediate, reflective), varied optical water characteristics (clear oceanic, estuarine turbid, macro-algal), and distinct breaker classifications (spilling, plunging, surging, collapsing). Training a foundation vision model (e.g., Vision Transformers or large-scale convolutional backbones) on this multi-site benchmark could enable universal zero-shot roller segmentation. This would streamline data pipelines by completely eliminating the operational latency and human effort associated with localized training and manual pixel-level annotation.

3. **Novel Direct Georeferencing and Photogrammetric Rectification Beyond the Surf Zone:** A persistent geometric bottleneck in coastal optical remote sensing is the geographic limitation of Ground Control Points (GCPs), which are necessarily restricted to the subaerial beach. As a result, photogrammetric transformation precision degrades monotonically with cross-shore distance ($X > 300$–$400\,\mathrm{m}$), amplifying projection uncertainties over the outer bar and offshore shoaling zone (Turner et al., 2016). To resolve this constraint without hazardous marine instrument deployments, three advanced non-intrusive georeferencing strategies should be investigated:

    - *Direct Georeferencing via RTK/PPK GNSS and IMU Integration:* Utilizing dual-frequency Real-Time Kinematic (RTK) or Post-Processed Kinematic (PPK) UAV positioning coupled with high-precision calibrated Inertial Measurement Units (IMUs) to solve absolute external camera orientations independently of terrestrial ground targets.
    - *Horizon-Based Pitch/Roll Optimization and Geometric Rays:* Leveraging the optical sea-horizon line within wide-angle oblique imagery as an absolute spatial boundary constraint to correct camera attitude drift, dynamically updating the projection matrix across turbulent wind gusts.
    - *Deployable Smart GNSS Drifter Arrays:* Utilizing compact, floating Lagrangian surface drifters equipped with high-accuracy GNSS receivers anchored seaward of the breaker line to serve as dynamic, floating ground-truth coordinates for offshore bundle adjustment.

4. **Stereoscopic Multi-Camera UAV Arrays and 3D Free-Surface Reconstruction:** The current formulation assumes a canonical wave-face inclination ($\theta \approx 15^\circ$) based on quasi-steady empirical literature. To eliminate this parametric assumption, future aerial platforms should integrate synchronized multi-camera stereoscopic baselines or lightweight airborne topobathymetric LiDAR. Resolving the true three-dimensional surface elevation profile of the breaking

wave ($\eta(x, y, t)$) in real time will enable the direct volumetric integration of roller fluid mass, capturing localized steepness variations during violent plunging impacts and establishing an exact, unparameterized mechanical dissipation balance.

ACKNOWLEDGMENTS

The authors gratefully acknowledge the financial support provided by the Agencia Nacional de Investigación y Desarrollo (ANID) through FONDECYT Regular Project No. 1231494, "The fate of freshwater in the surfzone: assessing the roles of the short and long wave forcing". Additionally, this research was supported by the *Programa de Incentivo a la Iniciación Científica* (PIIC) from Universidad Técnica Federico Santa María.

We also extend our gratitude to the *Empresa Portuaria San Antonio* (EPSA) for providing the in-situ ADCP wave records essential for the validation of this study.

BIBLIOGRAPHY

Almar, R., Cienfuegos, R., Catalán, P. A., Michallet, H., Castelle, B., Bonneton, P., & Marieu, V. (2012). A new breaking wave height direct estimator from video imagery. *Coastal Engineering*, *61*, 42–48. https://doi.org/10.1016/j.coastaleng.2011.12.004

Apotsos, A., Raubenheimer, B., Elgar, S., Guza, R. T., & Smith, J. A. (2007). Effects of wave rollers and bottom stress on wave setup. *Journal of Geophysical Research: Oceans*, *112*(C2), C02003. https://doi.org/10.1029/2006JC003549

Barbier, E. B., Hacker, S. D., Kennedy, C., Koch, E. W., Stier, A. C., & Silliman, B. R. (2011). The value of estuarine and coastal ecosystem services. *Ecological Monographs*, *81*(2), 169–193. https://doi.org/10.1890/10-1510.1

Battjes, J. A., & Janssen, J. P. F. M. (1978). Energy loss and set-up due to breaking of random waves. *Proceedings of the 16th International Conference on Coastal Engineering (ICCE 1978)*, 569–587. https://doi.org/10.9753/icce.v16.32

Bergsma, E. W. J., Almar, R., de Almeida, L. P. M., & Sall, M. (2019). On the operational use of UAVs for video-derived bathymetry. *Coastal Engineering*, *152*, 103527. https://doi.org/10.1016/j.coastaleng.2019.103527

Bergsma, E. W. J., Almar, R., de Vries, S., & Aarninkhof, S. G. J. (2016). Video-based nearshore bathymetry estimation in a macro-tidal environment. *Marine Geology*, *374*, 31–41. https://doi.org/10.1016/j.margeo.2016.02.001

Besset, M., Anthony, E. J., & Bouchette, F. (2019). Multi-decadal variations in delta shorelines and their relationship to river sediment supply: An assessment and review. *Earth-Science Reviews*, *193*, 199–219. https://doi.org/10.1016/j.earscirev.2019.04.018

Booij, N., Ris, R. C., & Holthuijsen, L. H. (1999). A third-generation wave model for coastal regions: 1. model description and validation. *Journal of Geophysical Research: Oceans*, *104*(C4), 7649–7666. https://doi.org/10.1029/98JC02622

Bradski, G. (2000). The OpenCV library. *Dr. Dobb's Journal of Software Tools*, *25*(11), 120–125.

Brodie, K. L., Bruder, B. L., Slocum, R. K., & Spore, N. J. (2019). Simultaneous mapping of coastal topography and bathymetry from a lightweight multicamera UAS. *IEEE Transactions on Geoscience and Remote Sensing*, *57*(9), 6844–6864. https://doi.org/10.1109/TGRS.2019.2909026

Bruder, B. L., & Brodie, K. L. (2020). CIRN quantitative coastal imaging toolbox. *SoftwareX*, *12*, 100582. https://doi.org/10.1016/j.softx.2020.100582

Buscombe, D., & Carini, R. J. (2019). A data-driven approach to classifying wave breaking in infrared imagery. *Remote Sensing*, *11*(7), 859. https://doi.org/10.3390/rs11070859

Castelle, B., & Masselink, G. (2022). Morphodynamics of wave-dominated beaches. *Cambridge Prisms: Coastal Futures*, *1*, e1. https://doi.org/10.1017/cft.2022.2

Catalán, P. A., & Haller, M. C. (2008). Remote sensing of breaking wave phase speeds with application to non-linear depth inversions. *Coastal Engineering*, *55*(2), 93–111. https://doi.org/10.1016/j.coastaleng.2007.06.004

Catalán, P. A., Haller, M. C., Holman, R. A., & Plant, W. J. (2011). Optical and microwave detection of wave breaking in the surf zone. *IEEE Transactions on Geoscience and Remote Sensing*, *49*(6), 1879–1893. https://doi.org/10.1109/TGRS.2010.2095864

Chawla, A., & Kirby, J. T. (2002). Monochromatic and random wave transformation at a river mouth. *Journal of Geophysical Research: Oceans*, *107*(C7), 3067. https://doi.org/10.1029/2001JC001042

Chen, J., Raubenheimer, B., & Elgar, S. (2024). Wave and roller transformation over barred bathymetry. *Journal of Geophysical Research: Oceans*, *129*(5), e2023JC020413. https://doi.org/10.1029/2023JC020413

Coco, G., Senechal, N., Rejas, A., Bryan, K. R., Capo, S., MacMahan, J. H., Ruessink, B. G., & Ward, T. I. (2014). Contemporary morphodynamics: The good, the bad and the ugly. *Marine Geology*, *352*, 434–453. https://doi.org/10.1016/j.margeo.2014.01.003

Dally, W. R., Dean, R. G., & Dalrymple, R. A. (1985). A model for wave height transformation on beaches. *Journal of Geophysical Research: Oceans*, *90*(C6), 11917–11927. https://doi.org/10.1029/JC090iC06p11917

Dean, R. G., & Dalrymple, R. A. (1991). *Water wave mechanics for engineers and scientists* (Vol. 2). World Scientific. https://doi.org/10.1142/1232

Díaz, H., Catalán, P. A., & Wilson, G. W. (2018). Quantification of two-dimensional wave breaking dissipation in the surf zone from remote sensing data. *Remote Sensing*, *10*(1), 38. https://doi.org/10.3390/rs10010038

Díez, M., Sierra, J. P., Redondo, J. M., Mósso, C., & Bezerra, M. O. (1999). Estudio hidrodinámico de la zona costera mediante el análisis digital de imágenes. *Ingeniería del Agua*, *6*(3), 283–292. https://doi.org/10.4995/ia.1999.2793

Duncan, J. H. (1981). An experimental investigation of breaking waves produced by a towed hydrofoil. *Proceedings of the Royal Society of London. Series A, Mathematical and Physical Sciences*, *377*(1770), 331–348. https://doi.org/10.1098/rspa.1981.0127

Feddersen, F. (2014). The generation of surfzone eddies in a strong alongshore current. *Journal of Physical Oceanography*, *44*(2), 600–617. https://doi.org/10.1175/JPO-D-13-051.1

Feddersen, F., Guza, R. T., Elgar, S., & Herbers, T. H. C. (1998). Alongshore momentum balances in the nearshore. *Journal of Geophysical Research: Oceans*, *103*(C8), 15667–15676. https://doi.org/10.1029/98JC01177

Feddersen, F., Olabarrieta, M., Guza, R. T., Winters, D., Raubenheimer, B., & Elgar, S. (2016). Observations and modeling of a tidal inlet dye tracer plume. *Journal of Geophysical Research: Oceans*, *121*(10), 7819–7844. https://doi.org/10.1002/2016JC011922

Flores, R. P., Catalán, P. A., & Haller, M. C. (2016). Estimating surfzone wave transformation and wave setup from remote sensing data. *Coastal Engineering*, *114*, 244–252. https://doi.org/10.1016/j.coastaleng.2016.04.008

Galbán-Malagón, C. J., Zapata, J., Perez-Venegas, D. J., Vargas, R., Latorre-Padilla, N., Luarte, T., Ahrendt, C., Hirmas-Olivares, A., Gómez-Aburto, V., Tapia, P., Isamit, V., Arce, P., Sánchez, C., & Pozo, K. (2023). Occurrence, source estimation, and risk assessment of polycyclic aromatic hydrocarbons in coastal seawaters from the Quintero industrial complex (Valparaíso,

Chile). *Science of the Total Environment*, *878*, 162957. https://doi.org/10.1016/j.scitotenv.2023.162957

Gómez, V., Torres, M., Karásková, P., Přibylová, P., Klánová, J., & Pozo, K. (2021). Occurrence of perfluoroalkyl substances (PFASs) in marine plastic litter from coastal areas of central Chile. *Marine Pollution Bulletin*, *172*, 112818. https://doi.org/10.1016/j.marpolbul.2021.112818

Grossmann, F., Streßer, M., Raubenheimer, B., & Elgar, S. (2026). Radar estimates of surfzone dissipation drive a morphological evolution model. *Geophysical Research Letters*, *53*, e2025GL119305. https://doi.org/10.1029/2025GL119305

Guimarães, P. V., Stringari, C. E., Filipot, J.-F., Leckler, F., Benetazzo, A., & Chapron, B. (2026). Geometry of breaking waves under natural sea conditions. *Geophysical Research Letters*, *53*, e2026GL122293. https://doi.org/10.1029/2026GL122293

Herbers, T. H. C., Elgar, S., & Guza, R. T. (1999). Directional spreading of waves in the nearshore. *Journal of Geophysical Research: Oceans*, *104*(C4), 7683–7693. https://doi.org/10.1029/1998JC900092

Holland, K. T., Holman, R. A., Lippmann, T. C., Stanley, J., & Plant, N. (1997). Practical use of video imagery in nearshore oceanographic field studies. *IEEE Journal of Oceanic Engineering*, *22*(1), 81–92. https://doi.org/10.1109/48.557542

Holman, R. A., & Stanley, J. (2007). The history and technical capabilities of Argus. *Coastal Engineering*, *54*(6-7), 477–491. https://doi.org/10.1016/j.coastaleng.2007.01.003

Janssen, T. T., & Battjes, J. A. (2007). A note on wave height distributions in shallow water. *Coastal Engineering*, *54*(9), 715–725. https://doi.org/10.1016/j.coastaleng.2007.05.004

Lai, R. J., & Cairns, J. L. (1998). Wave-current interaction at an inlet. *OCEANS '98 Conference Proceedings*, *3*, 1604–1608. https://doi.org/10.1109/OCEANS.1998.726296

Lippmann, T. C., & Holman, R. A. (1991). Phase speed and angle of breaking waves in the surf zone from video imagery. *Journal of Geophysical Research: Oceans*, *96*(C6), 11641–11654. https://doi.org/10.1029/91JC00529

Liu, G., Cai, F., Qi, H., Liu, J., Zhu, J., Cao, C., & Lei, G. (2024). Decadal evolution of a sandy beach adjacent to a river mouth under natural drivers and human impacts. *Frontiers in Marine Science*, *11*, 1384780. https://doi.org/10.3389/fmars.2024.1384780

Longuet-Higgins, M. S., & Stewart, R. W. (1964). Radiation stresses in water waves; a physical discussion, with applications. *Deep Sea Research and Oceanographic Abstracts*, *11*(4), 529–562. https://doi.org/10.1016/0011-7471(64)90001-4

Mardia, K. V., & Jupp, P. E. (2000). *Directional statistics*. John Wiley & Sons. https://doi.org/10.1002/9780470316979

Martínez, C., & Saldías, G. S. (2023). Campaña científica investiga posibles causas tras el cierre de la desembocadura del río Maipo.

Olabarrieta, M., Medina, R., & Lomónaco Tonda, P. (2005). Efecto de la interacción ola-corriente en la propagación de la marea en estuarios. *Ingeniería del Agua*, *12*(4), 329–340. https://doi.org/10.4995/ia.2005.2569

Olabarrieta, M., Warner, J. C., & Kumar, N. (2011). Wave-current interaction in Willapa Bay. *Journal of Geophysical Research: Oceans*, *116*(C12), C12014. https://doi.org/10.1029/2011JC007387

Peregrine, D. H. (1976). Interaction of water waves and currents. *Advances in Applied Mechanics*, *16*, 9–117. https://doi.org/10.1016/S0065-2156(08)70087-5

Perlin, M., Choi, W., & Tian, Z. (2013). Breaking waves in deep and intermediate waters. *Annual Review of Fluid Mechanics*, *45*, 115–145. https://doi.org/10.1146/annurev-fluid-011212-140721

Phillips, O. M. (1977). *The dynamics of the upper ocean* (2nd). Cambridge University Press.

QGIS Development Team. (2024). *QGIS geographic information system*. QGIS Association. https://www.qgis.org

Ranasinghe, R. (2016). Assessing climate change impacts on open sandy coasts: A review. *Earth-Science Reviews*, *160*, 320–332. https://doi.org/10.1016/j.earscirev.2016.07.011

Roco, A., Flores, R. P., Williams, M. E., & Saldías, G. S. (2024). Observations of river-wave interactions at a small-scale river mouth. *Coastal Engineering*, *189*, 104456. https://doi.org/10.1016/j.coastaleng.2024.104456

Rodriguez, A. R., Giddings, S. N., & Kumar, N. (2018). Impacts of nearshore wave-current interaction on transport and mixing of small-scale buoyant plumes. *Geophysical Research Letters*, *45*(16), 8379–8389. https://doi.org/10.1029/2018GL078328

Roelvink, D., Reniers, A., van Dongeren, A., van Thiel de Vries, J., McCall, R., & Lescinski, J. (2009). Modelling storm impacts on beaches, dunes and barrier islands. *Coastal Engineering*, *56*(11-12), 1133–1152. https://doi.org/10.1016/j.coastaleng.2009.08.006

Rojas, C. M., Saldías, G. S., Flores, R. P., Vásquez, S. I., Salas, C., & Vargas, C. A. (2023). A modeling study of hydrographic and flow variability along the river-influenced coastal ocean off central Chile. *Ocean Modelling*, *181*, 102155. https://doi.org/10.1016/j.ocemod.2022.102155

Ruessink, B. G., Miles, J. R., Ranasinghe, R., Phillips, M. R., & Davidson, M. A. (2001). Modeling cross-shore wave dissipation in the surf zone: A test of the roller concept. *Continental Shelf Research*, *21*(15), 1577–1597. https://doi.org/10.1016/S0278-4343(01)00021-3

Sáez, F. J., Catalán, P. A., & Valle, C. (2021). Wave-by-wave nearshore wave breaking identification using U-Net. *Coastal Engineering*, *170*, 104021. https://doi.org/10.1016/j.coastaleng.2021.104021

Sáez, F. J., Catalán, P. A., Valle, C., Spicer Bak, A., Flores, R. P., Fournier, F., & Veliz, S. (2026). A generalized method based on transfer learning and human-in-the-loop for wave-by-wave identification of nearshore wave breaking patterns. *Coastal Engineering*, *In Press*, 104954. https://doi.org/10.1016/j.coastaleng.2026.104954

Schäffer, H. A., Madsen, P. A., & Deigaard, R. (1993). A Boussinesq model for waves breaking in shallow water. *Coastal Engineering*, *20*(3-4), 185–202. https://doi.org/10.1016/0378-3839(93)90001-O

Spalding, M. D., Ruffo, S., Lacambra, C., Meliane, I., Hale, L. Z., Shepard, C. C., & Beck, M. W. (2014). The role of ecosystems in coastal protection: Adapting to climate change and coastal hazards. *Ocean & Coastal Management*, *90*, 50–57. https://doi.org/10.1016/j.ocecoaman.2013.09.007

Stive, M. J. F., & de Vriend, H. J. (1994). Shear stresses and mean flow in shoaling and breaking waves. *Proceedings of the 24th International Conference on Coastal Engineering (ICCE 1994)*, *1*, 599–613. https://doi.org/10.9753/icce.v24.4985

Stringari, C. E., Harris, D. L., & Power, H. E. (2019). A novel machine learning algorithm for tracking remotely sensed waves in the surf zone. *Coastal Engineering*, *147*, 149–158. https://doi.org/10.1016/j.coastaleng.2019.02.002

Stringari, C. E., Power, H. E., & Harris, D. L. (2021). Remote sensing of coastal hydrodynamic processes using unmanned aerial vehicles (UAVs): A review. *Earth-Science Reviews*, *218*, 103673. https://doi.org/10.1016/j.earscirev.2021.103673

Svendsen, I. A. (1984). Wave heights and set-up in a surf zone. *Coastal Engineering*, *8*(4), 303–329. https://doi.org/10.1016/0378-3839(84)90028-0

Thornton, E. B., & Guza, R. T. (1983). Transformation of wave height distribution. *Journal of Geophysical Research: Oceans*, *88*(C10), 5925–5938. https://doi.org/10.1029/JC088iC10p05925

Toimil, A., Losada, I. J., Camus, P., & Díaz-Simal, P. (2017). Managing coastal erosion under climate change at the regional scale. *Coastal Engineering*, *128*, 106–122. https://doi.org/10.1016/j.coastaleng.2017.08.004

Turner, I. L., Harley, M. D., & Drummond, C. D. (2016). UAVs for coastal surveying. *Coastal Engineering*, *114*, 19–24. https://doi.org/10.1016/j.coastaleng.2016.03.011

US Army Corps of Engineers. (2002). *Coastal engineering manual* [Engineer Manual 1110-2-1100]. U.S. Army Corps of Engineers.

Warner, J. C., Armstrong, B., He, R., & Zambon, J. B. (2010). Development of a three-dimensional, coupled wave, current, and sediment-transport model: COAWST. *Ocean Modelling*, *35*(3), 230–244. https://doi.org/10.1016/j.ocemod.2010.07.010

Wright, L. D., & Short, A. D. (1984). Morphodynamic variability of surf zones and beaches: A synthesis. *Marine Geology*, *56*(1-4), 93–118. https://doi.org/10.1016/0025-3227(84)90008-2

Wu, Y., Zhang, Q., Liu, Z., & Ji, C. (2025). Experimental investigation on wave roller area evolution in the surf zone. *Applied Ocean Research*, *155*, 104460. https://doi.org/10.1016/j.apor.2025.104460

Xue, Q., Liang, S., Sun, Z., Xu, Y., & Tian, Z. (2023). Near-surface characteristics of velocity profile and momentum transport after wave-breaking in deep water. *Ocean Engineering*, *276*, 114223. https://doi.org/10.1016/j.oceaneng.2023.114223